Figure 1.


(a)
125°W
124°W
123°W
122°W
49°N
48°N
Nanaimo
Vancouver
Vancouver Island
Strait of Georgia
CANADA
UNTIED STATES
Port Renfrew
San Juan River
Juan de Fuca Strait
Victoria
Pacific Ocean
0 10 20 30 40 50
Kilometers
Yukon
Northwest Territories
British Columbia
Alberta
Saskatchewan
Pacific Ocean
San Juan River Watershed
CANADA
UNITED STATES
San Juan River watershed
International boundary
River
Lake
Basemap source:
Ministry of Natural Resources, Canada
2018
(b)
124°20'W
124°19'W
124°18'W
124°17'W
124°16'W
124°15'W
124°14'W
124°13'W
124°12'W
124°11'W
124°10'W
48°35'N
48°34'N
48°33'N
Harris Creek
Lens Creek
San Juan River
Red Creek
beginning of alluvial reach
WSC station
08HA010
Bar 15
0 100
Meters
Bar 7
Bar 6
0 200
Meters
0 1 2 3
Kilometers

Figure 2.

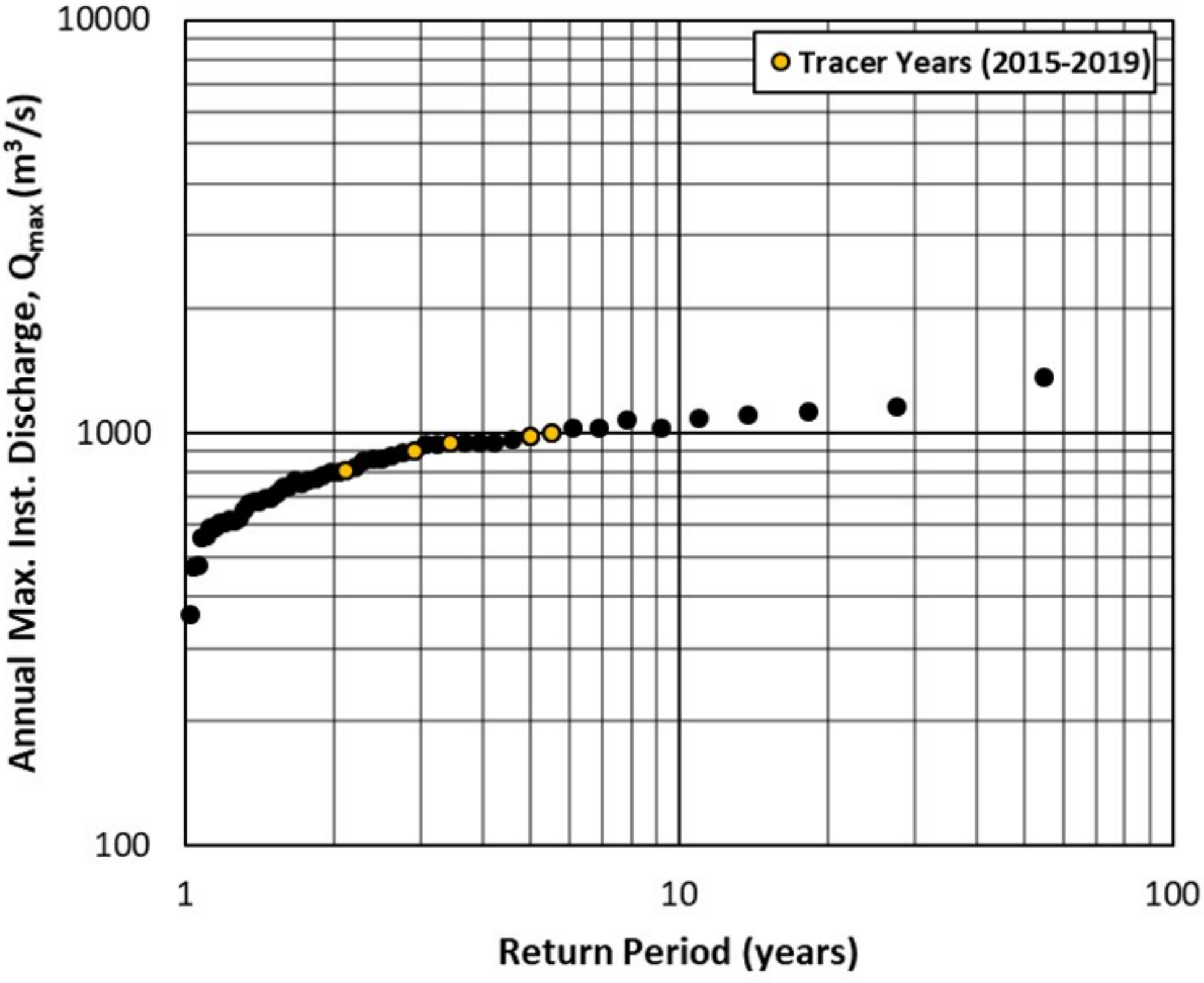
10000
1000
100
Annual Max. Inst. Discharge, Q_{max} (m^3/s)
Tracer Years (2015-2019)
1
10
100
Return Period (years)

Figure 3.

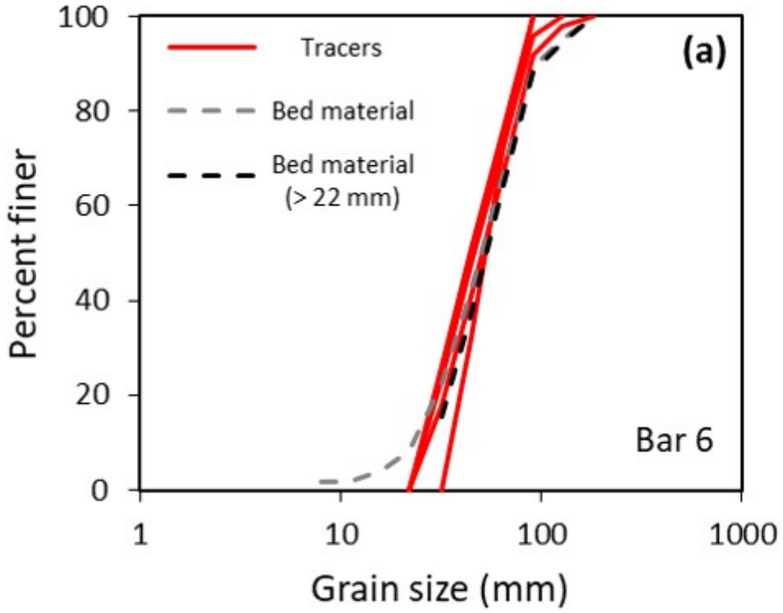
Tracers
Bed material
Bed material
(> 22 mm)
(a)
Bar 6
Percent finer
Grain size (mm)
100
80
60
40
20
0
1
10
100
1000

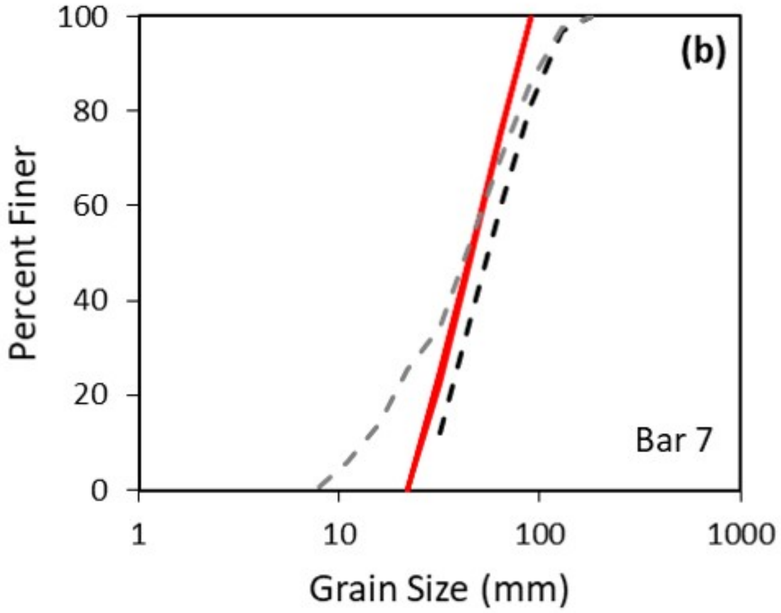
(b)
Bar 7
Percent Finer
Grain Size (mm)
100
80
60
40
20
0
1
10
100
1000

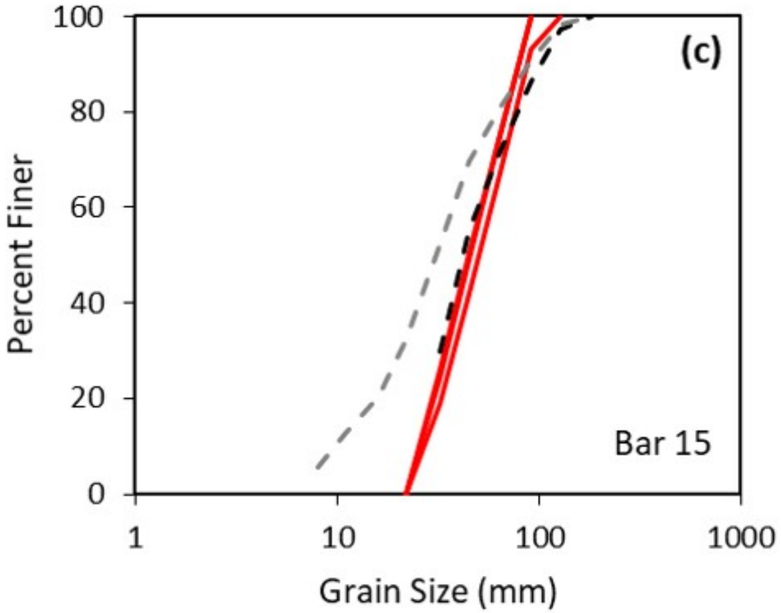
(c)
Bar 15
Percent Finer
Grain Size (mm)
100
80
60
40
20
0
1
10
100
1000

Figure 4.


(a)
(b)

Figure 5.


(a)
(b)

Figure 6.

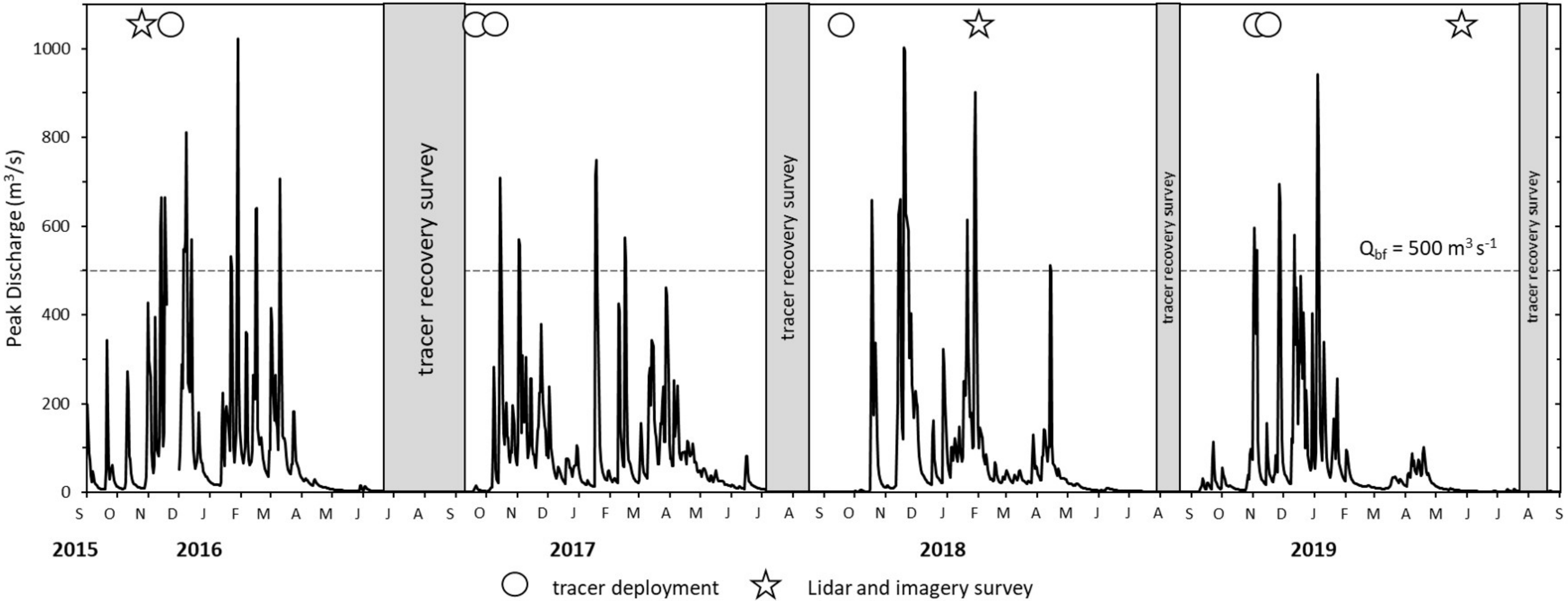
Peak Discharge (m³/s)
1000
800
600
400
200
0
tracer recovery survey
tracer recovery survey
tracer recovery survey
tracer recovery survey
Q_{bf} = 500 m³ s⁻¹
S O N D J F M A M J J A S O N D J F M A M J J A S O N D J F M A M J J A S O N D J F M A M J J A S
2015
2016
2017
2018
2019
tracer deployment
Lidar and imagery survey

Figure 7.

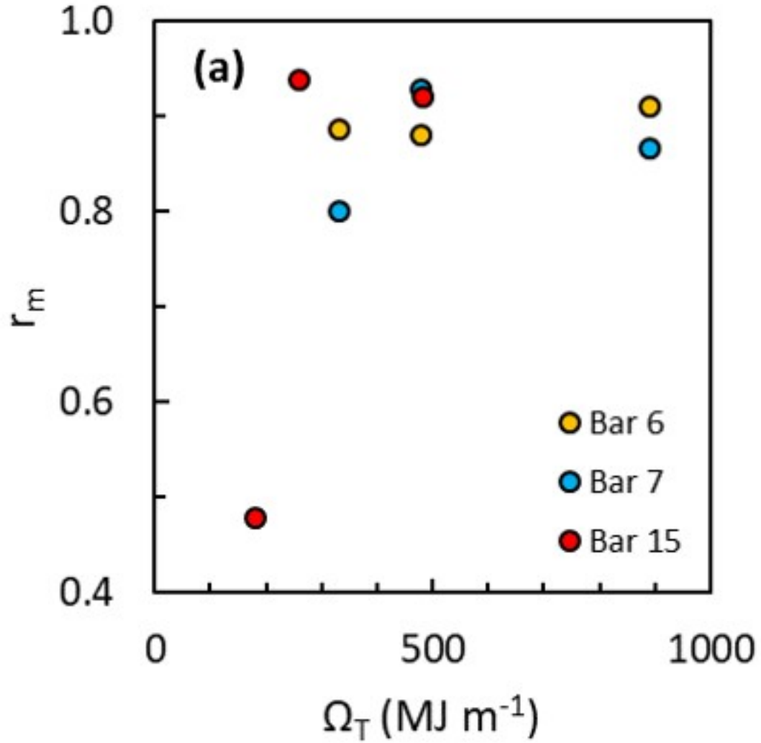
(a)
1.0
0.8
0.6
0.4
r_m
Bar 6
Bar 7
Bar 15
0
500
1000
Ω_T (MJ m^{-1})

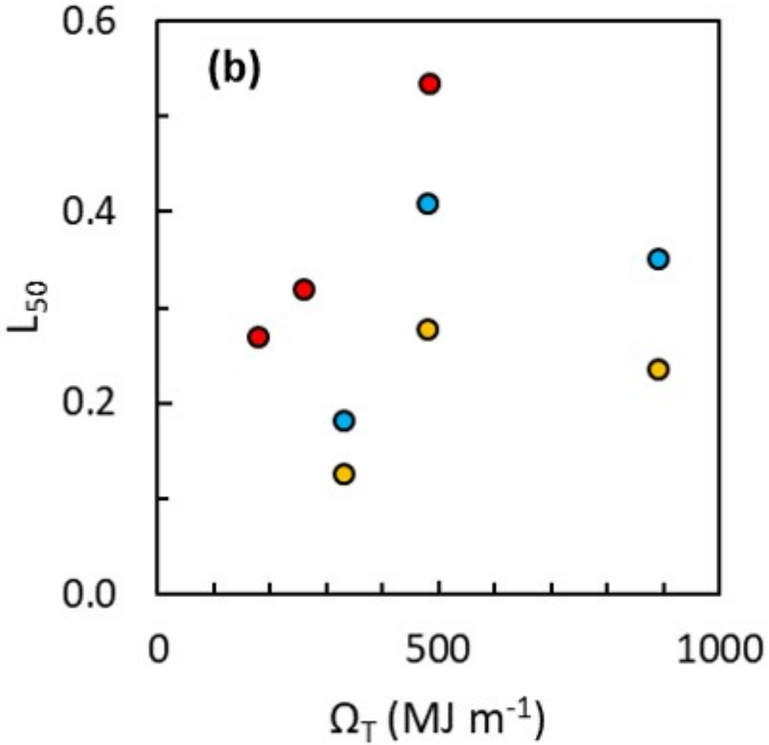
(b)
0.6
0.4
0.2
0.0
L_{50}
0
500
1000
Ω_T (MJ m^{-1})

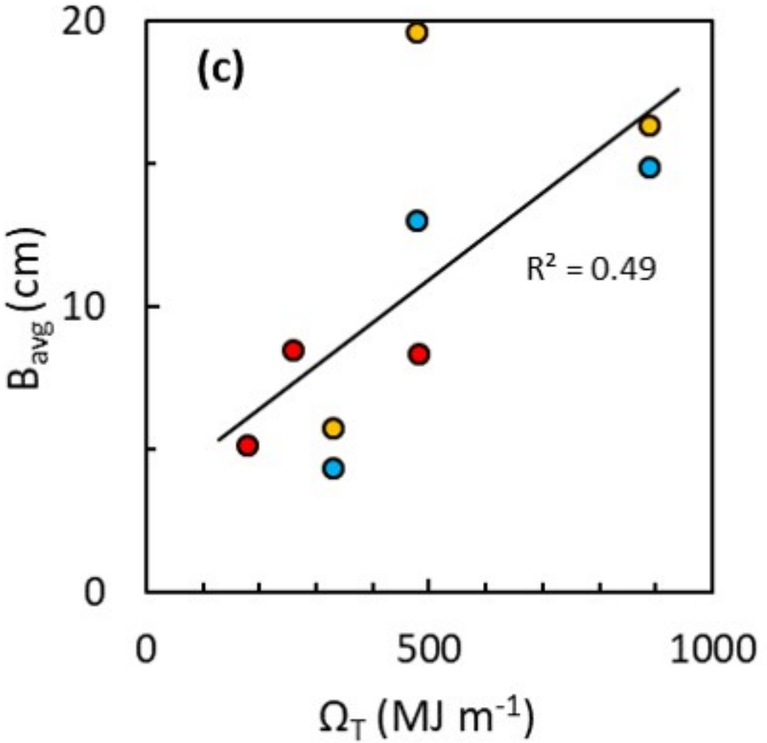
(c)
20
10
0
B_{avg} (cm)
R^2 = 0.49
0
500
1000
Ω_T (MJ m^{-1})

Figure 8.

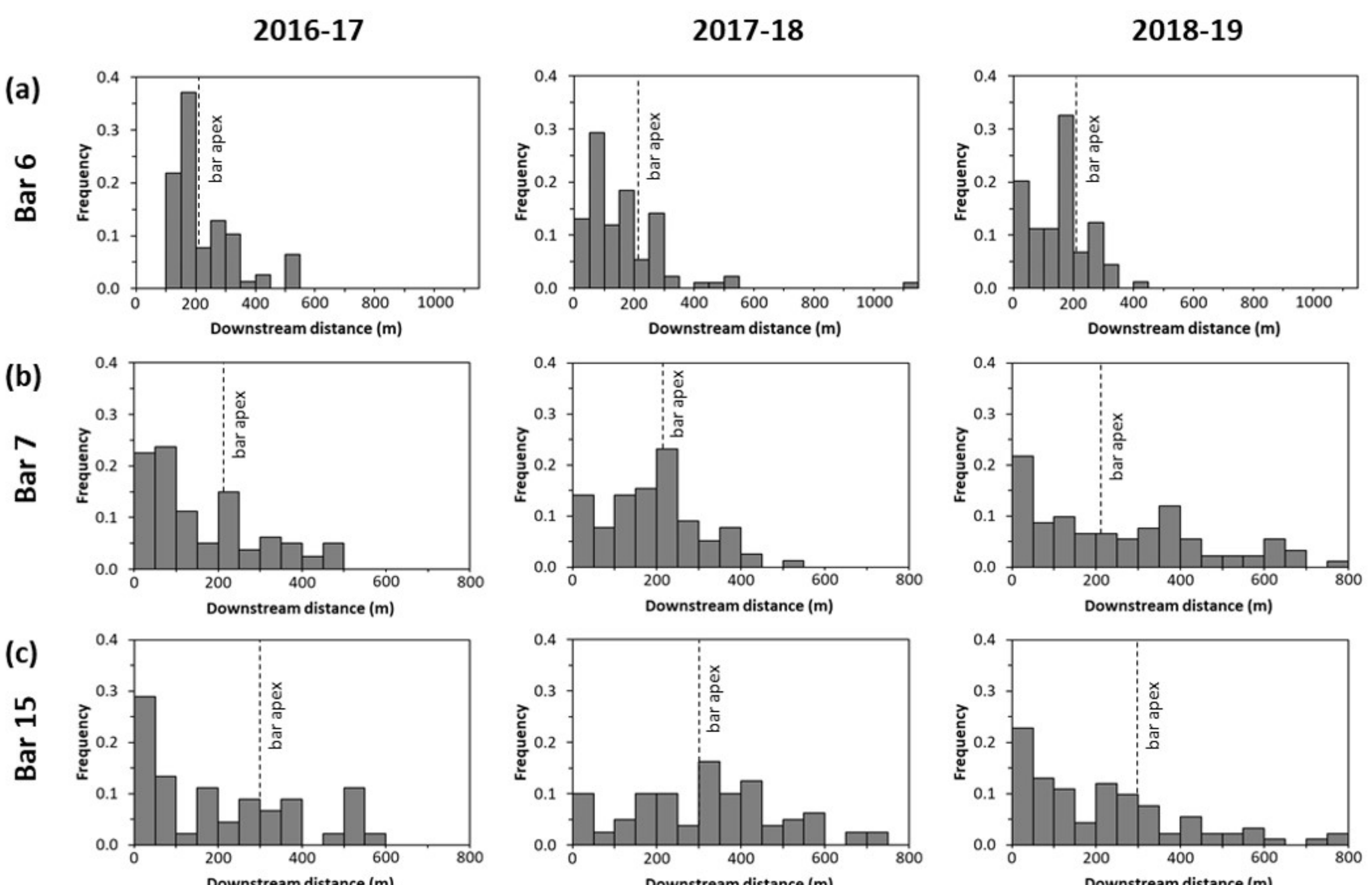
2016-17
2017-18
2018-19
(a)
Bar 6
(b)
Bar 7
(c)
Bar 15
Frequency
Downstream distance (m)
bar apex
0.0
0.1
0.2
0.3
0.4
0
200
400
600
800
1000

Figure 9.

(a)

Bar 6

Bar 5

2015 launch
2016 launch
2017 launch
2018 launch
Initial position of tracers

2015

(b)

N

Bar 6

Bar 5

2016

(c)

Bar 6

Bar 5

0 50 100 200

Meters

2017

(d)

Bar 6

Bar 5

2018

Figure 10.

(a)

2016

Bar 8

Bar 7

2016 launch
2017 launch
2018 launch
Initial position of tracers

N

(b)

2017

Bar 8

Bar 7

(c)

Bar 8

Bar 7

0 50 100 200

Meters

2018

Figure 11.

(a)

Bar 14

Bar 15

N

2016 launch
2017 launch
2018 launch
Initial position of tracers

2016

(b)

Bar 14

Bar 15

Bar 16

2017

(c)

Bar 14

Bar 15

Bar 16

0 50 100 200

Meters

2018

Figure 12.

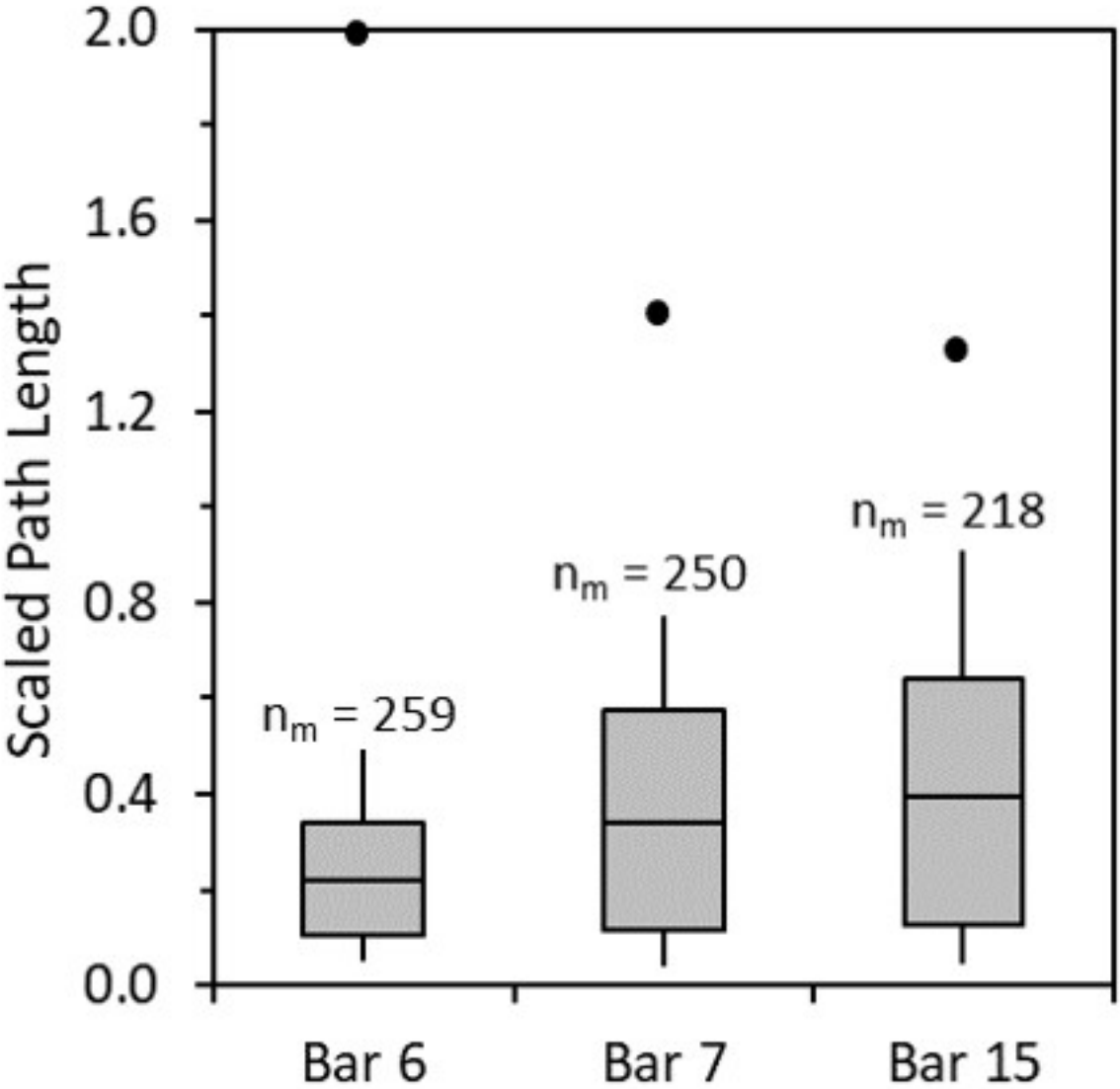
2.0
1.6
1.2
0.8
0.4
0.0
Scaled Path Length
n_m = 259
n_m = 250
n_m = 218
Bar 6
Bar 7
Bar 15

Figure 13.

Migrating
bedload sheet

Figure 14.

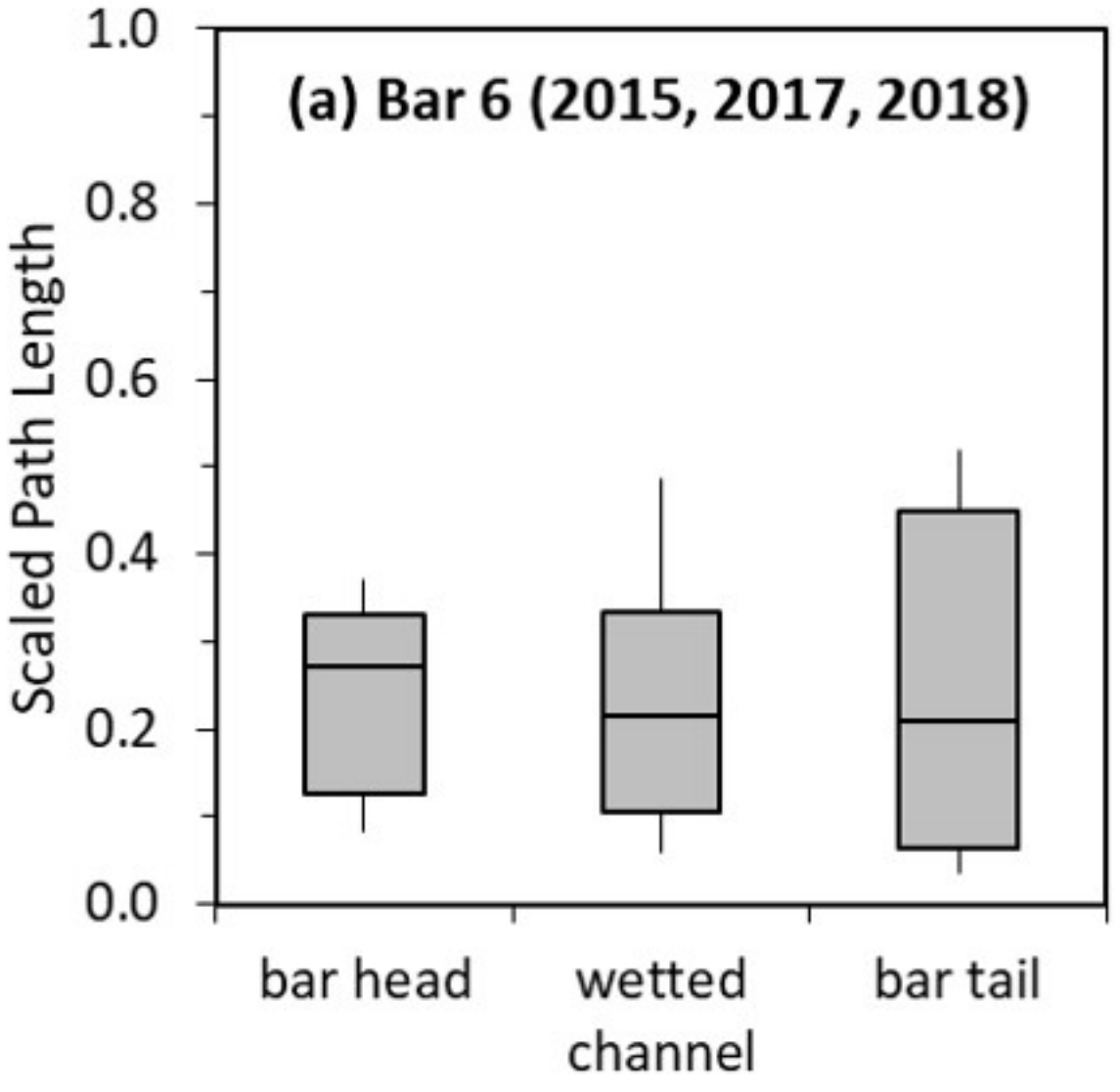
(a) Bar 6 (2015, 2017, 2018)
Scaled Path Length
1.0
0.8
0.6
0.4
0.2
0.0
bar head
wetted channel
bar tail

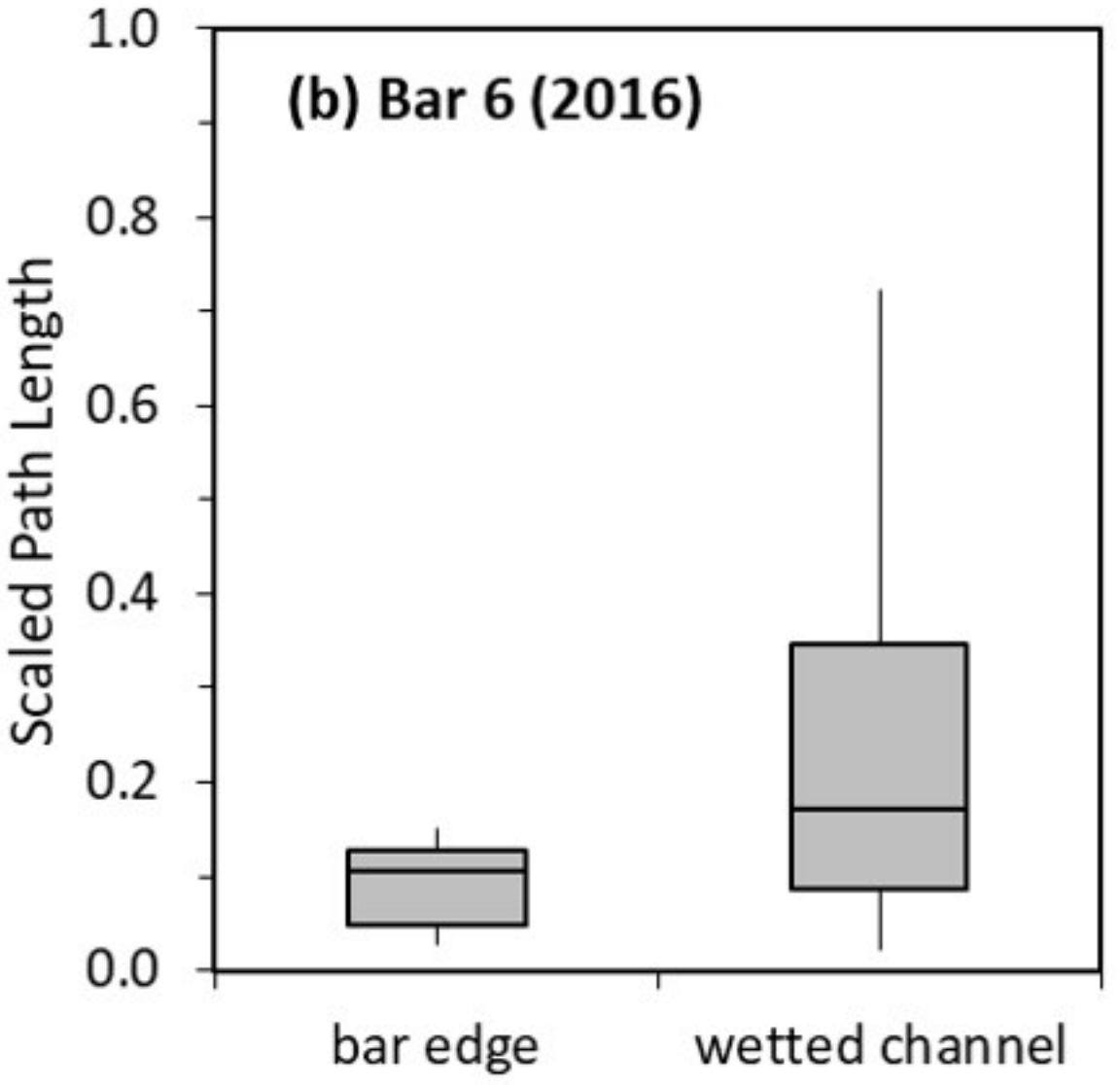
(b) Bar 6 (2016)
Scaled Path Length
1.0
0.8
0.6
0.4
0.2
0.0
bar edge
wetted channel

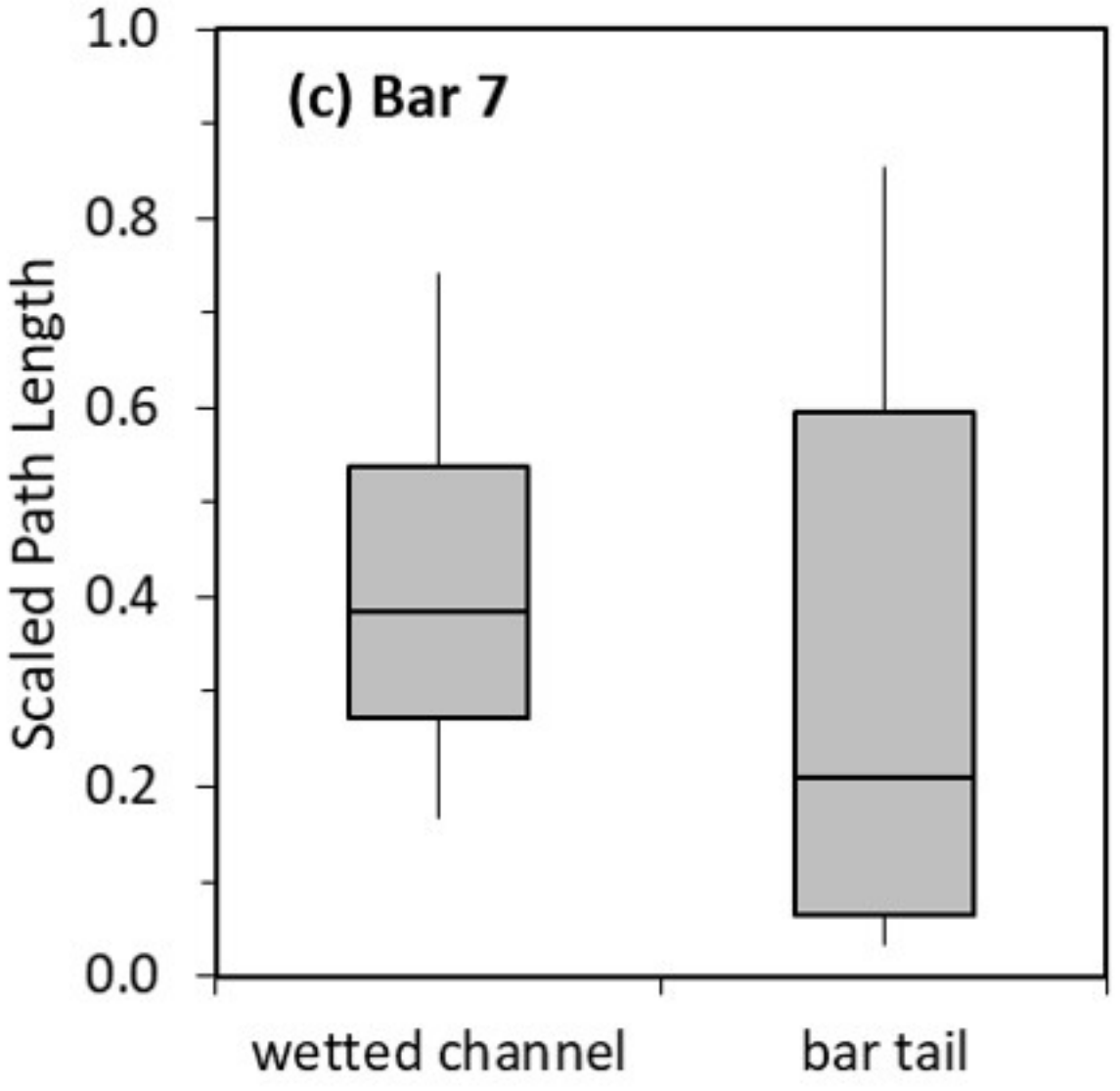
(c) Bar 7
Scaled Path Length
1.0
0.8
0.6
0.4
0.2
0.0
wetted channel
bar tail

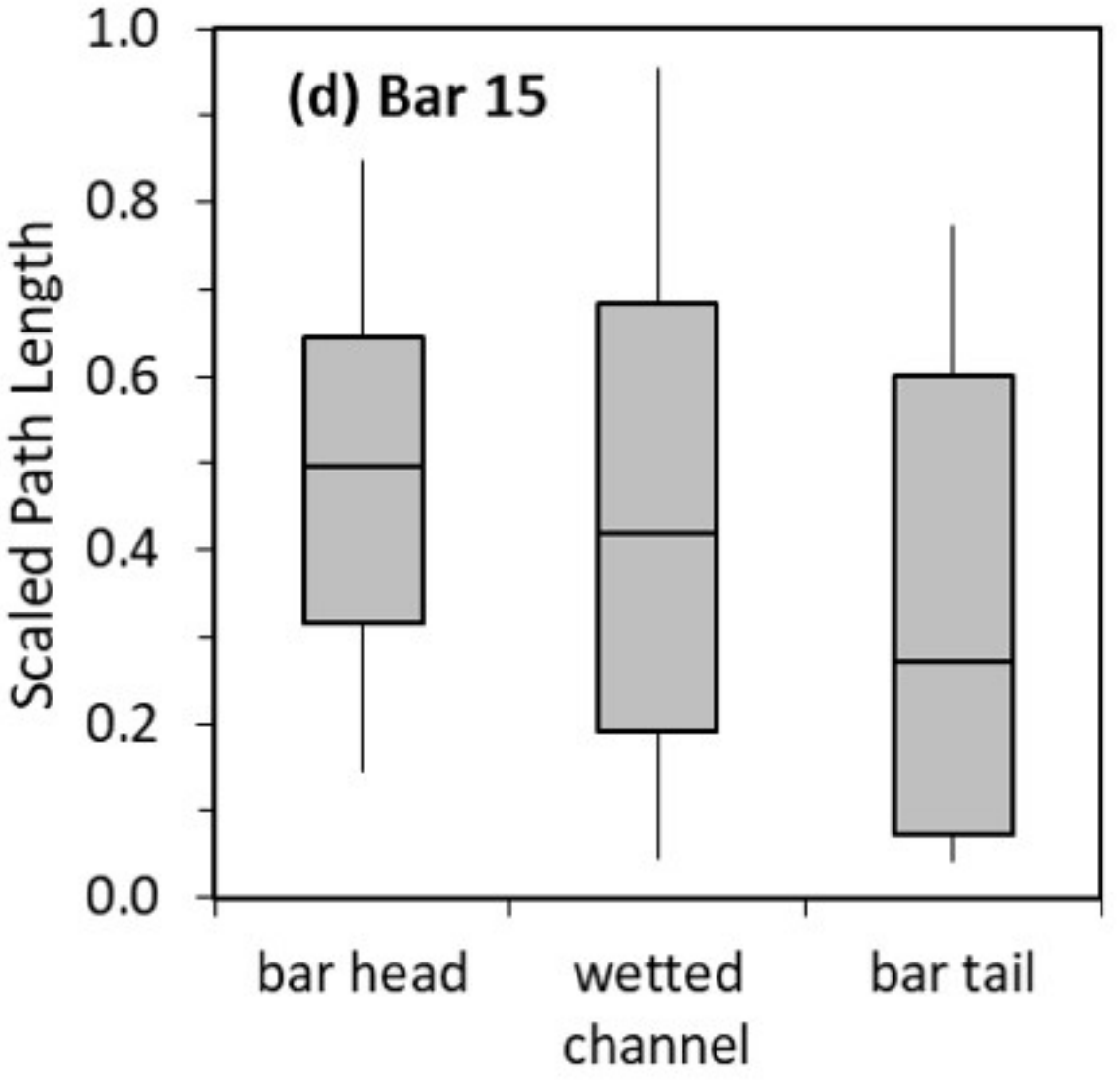
(d) Bar 15
Scaled Path Length
1.0
0.8
0.6
0.4
0.2
0.0
bar head
wetted channel
bar tail

Figure 15.

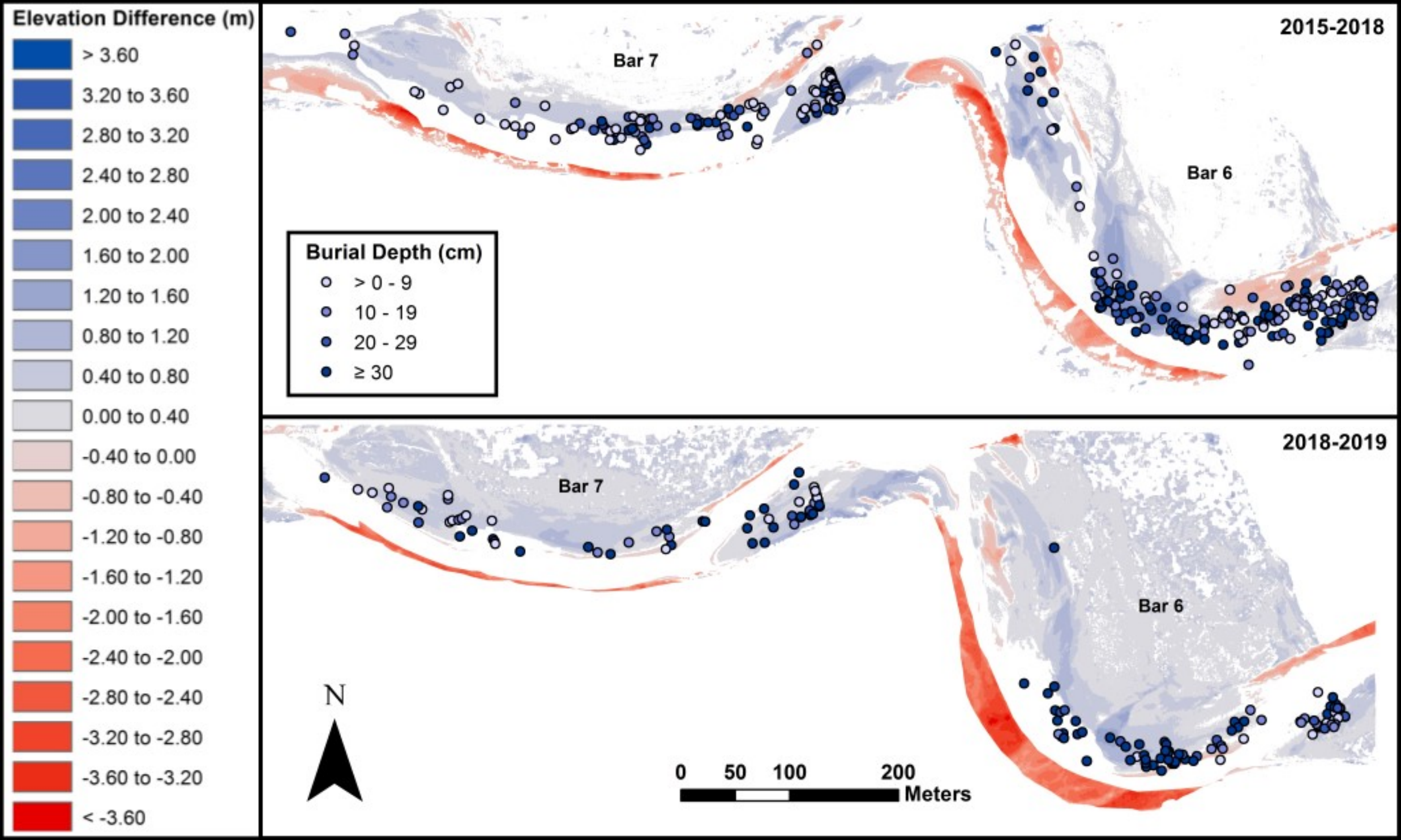
Elevation Difference (m)
> 3.60
3.20 to 3.60
2.80 to 3.20
2.40 to 2.80
2.00 to 2.40
1.60 to 2.00
1.20 to 1.60
0.80 to 1.20
0.40 to 0.80
0.00 to 0.40
-0.40 to 0.00
-0.80 to -0.40
-1.20 to -0.80
-1.60 to -1.20
-2.00 to -1.60
-2.40 to -2.00
-2.80 to -2.40
-3.20 to -2.80
-3.60 to -3.20
< -3.60
2015-2018
Bar 7
Bar 6
Burial Depth (cm)
> 0 - 9
10 - 19
20 - 29
≥ 30
2018-2019
Bar 7
Bar 6
N
0 50 100 200
Meters

Figure 16.

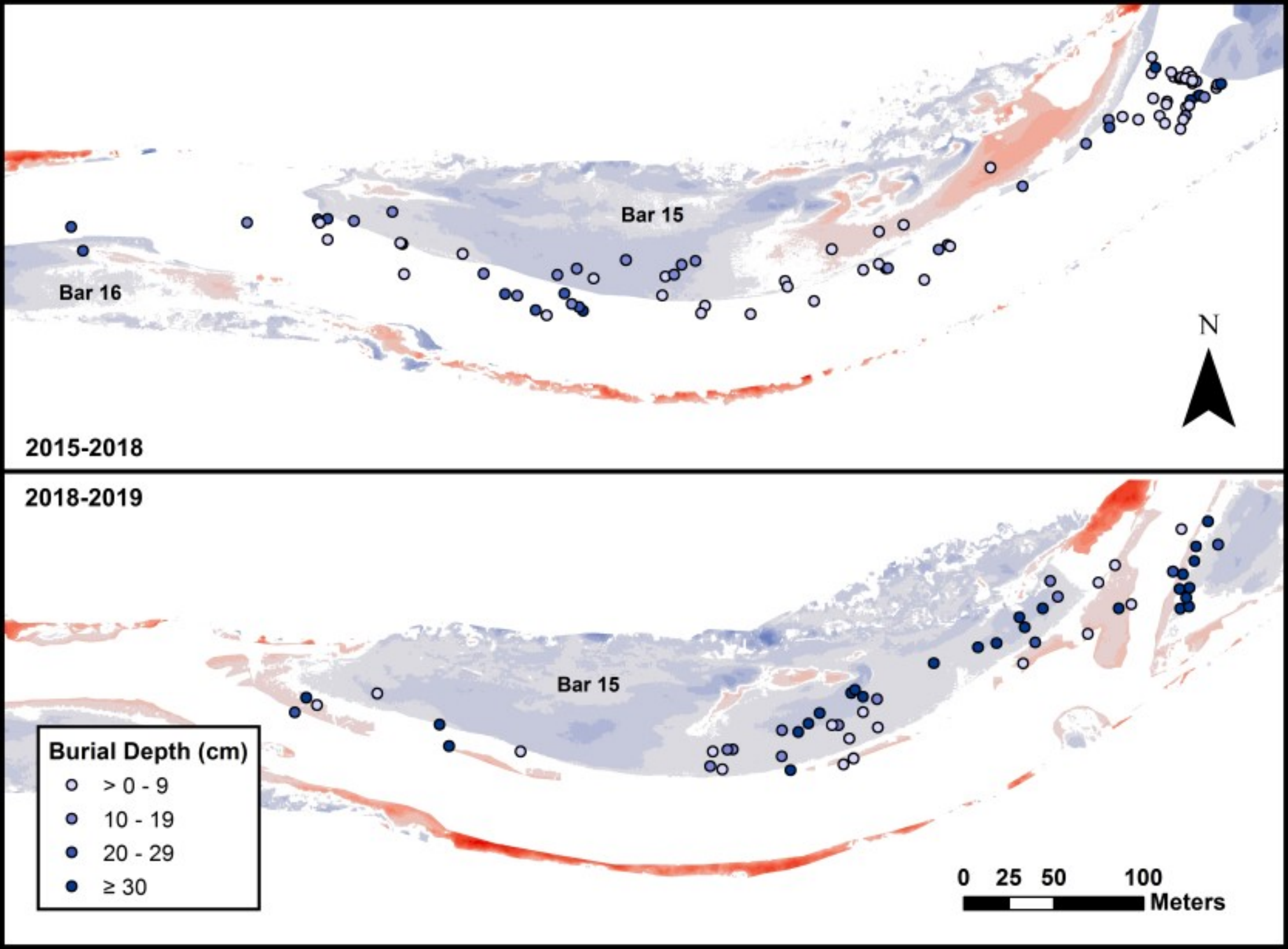
Bar 15
Bar 16
N
2015-2018
2018-2019
Bar 15
Burial Depth (cm)
> 0 - 9
10 - 19
20 - 29
≥ 30
0 25 50 100
Meters

Figure 17.

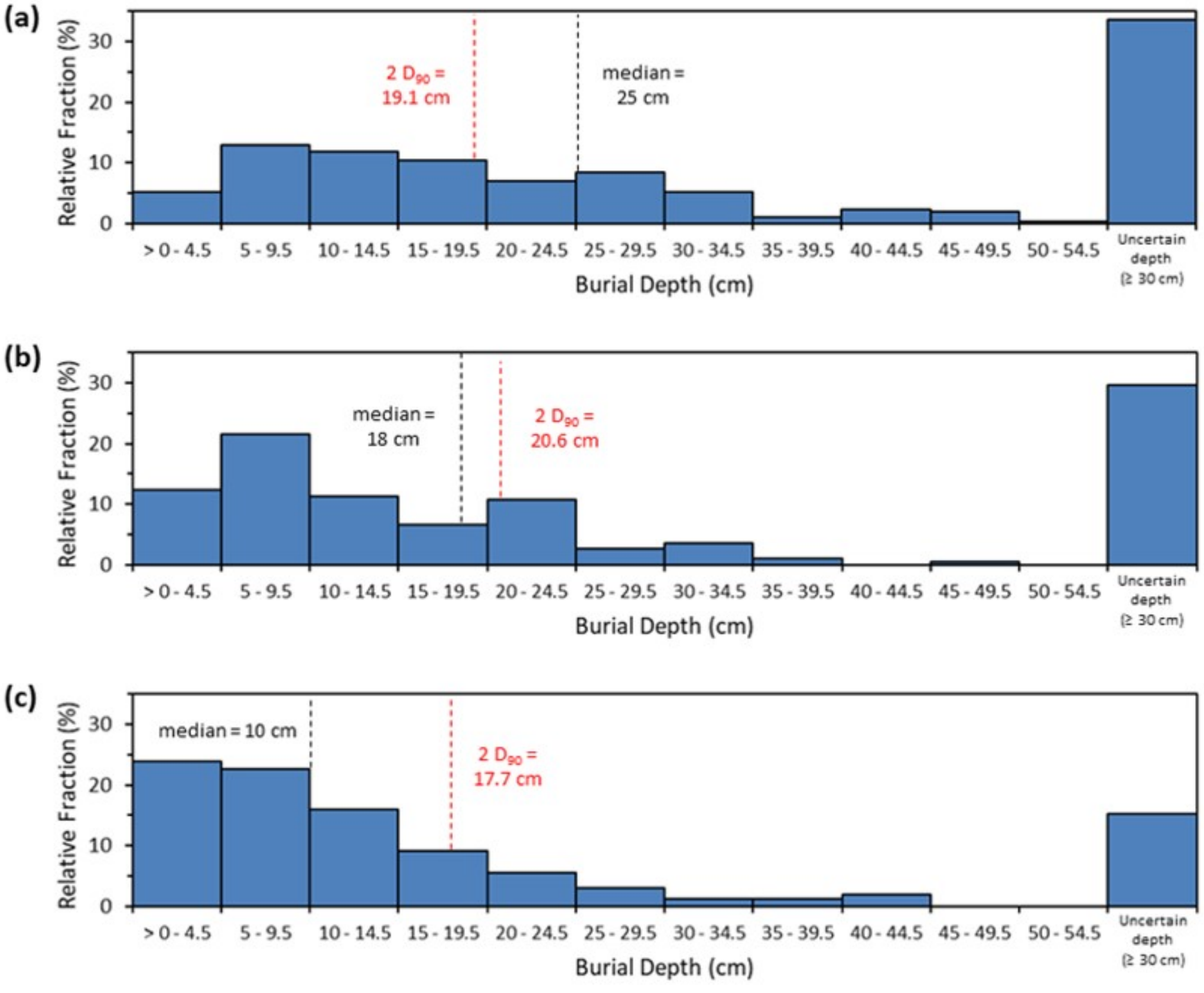
(a)
Relative Fraction (%)
30
20
10
0
2 D90 = 19.1 cm
median = 25 cm
> 0 - 4.5
5 - 9.5
10 - 14.5
15 - 19.5
20 - 24.5
25 - 29.5
30 - 34.5
35 - 39.5
40 - 44.5
45 - 49.5
50 - 54.5
Uncertain depth (≥ 30 cm)
Burial Depth (cm)
(b)
Relative Fraction (%)
30
20
10
0
median = 18 cm
2 D90 = 20.6 cm
> 0 - 4.5
5 - 9.5
10 - 14.5
15 - 19.5
20 - 24.5
25 - 29.5
30 - 34.5
35 - 39.5
40 - 44.5
45 - 49.5
50 - 54.5
Uncertain depth (≥ 30 cm)
Burial Depth (cm)
(c)
Relative Fraction (%)
30
20
10
0
median = 10 cm
2 D90 = 17.7 cm
> 0 - 4.5
5 - 9.5
10 - 14.5
15 - 19.5
20 - 24.5
25 - 29.5
30 - 34.5
35 - 39.5
40 - 44.5
45 - 49.5
50 - 54.5
Uncertain depth (≥ 30 cm)
Burial Depth (cm)

Figure 18.

(a) Bar 6

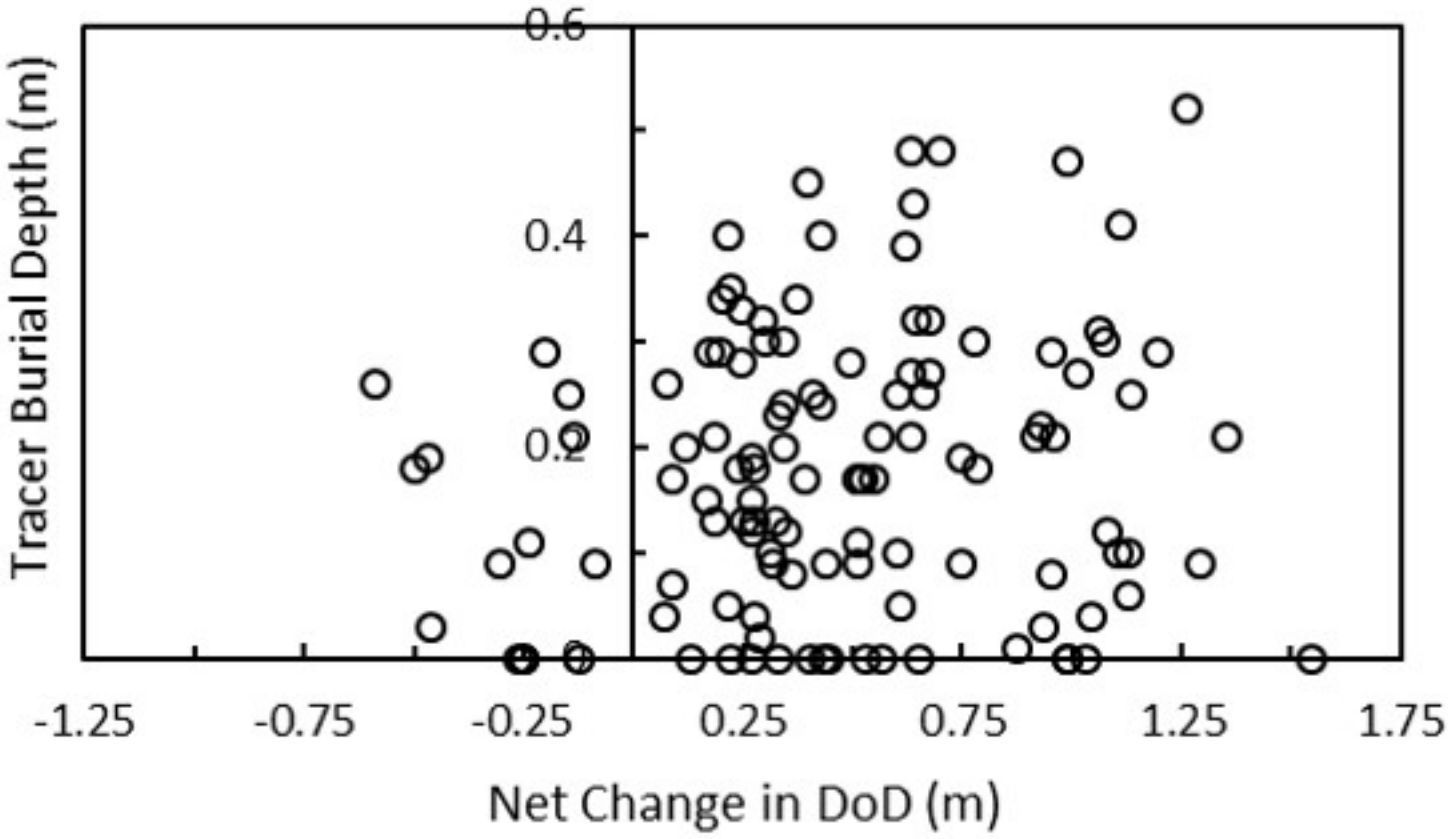

(b) Bar 7

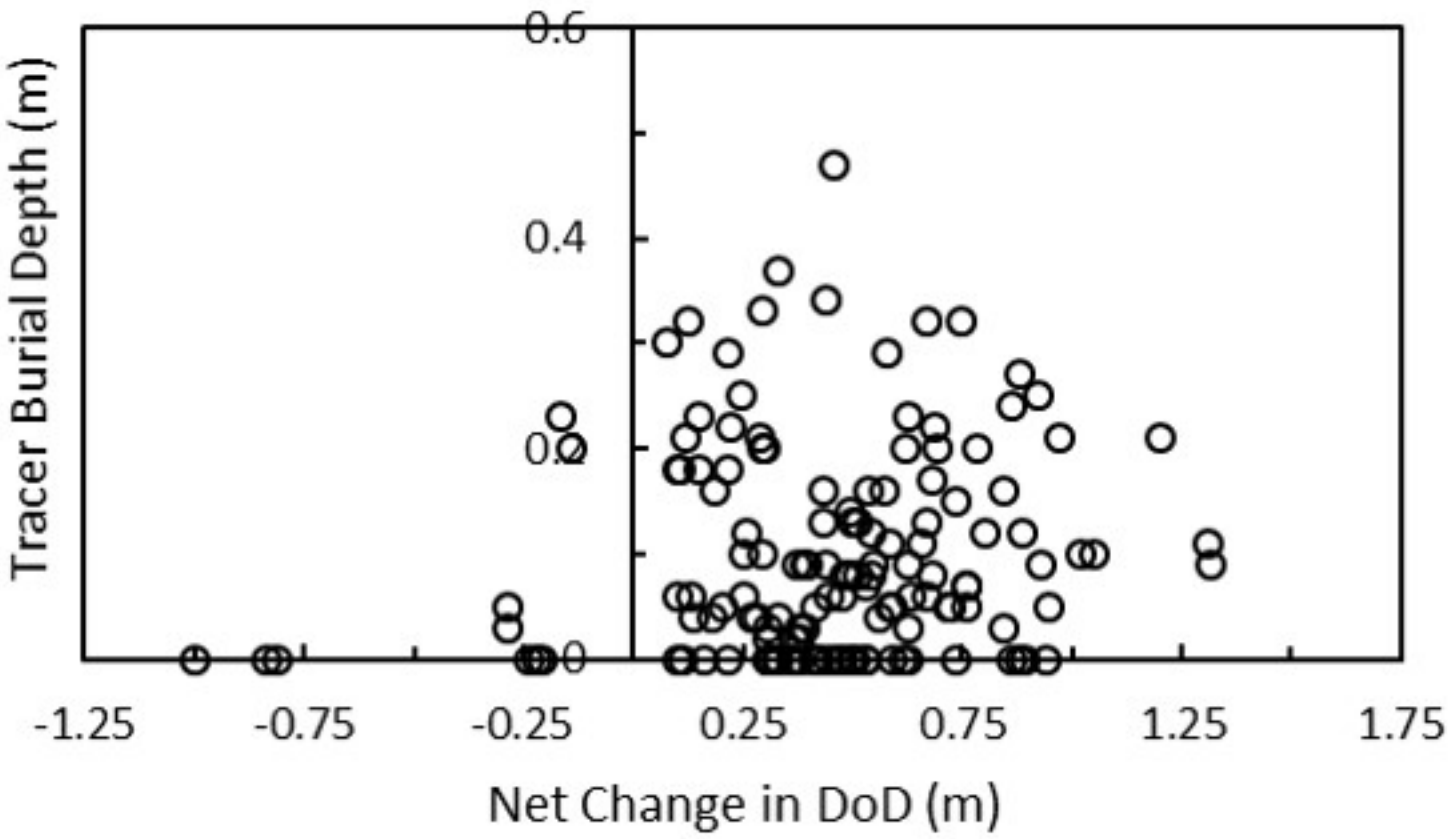

(b) Bar 15

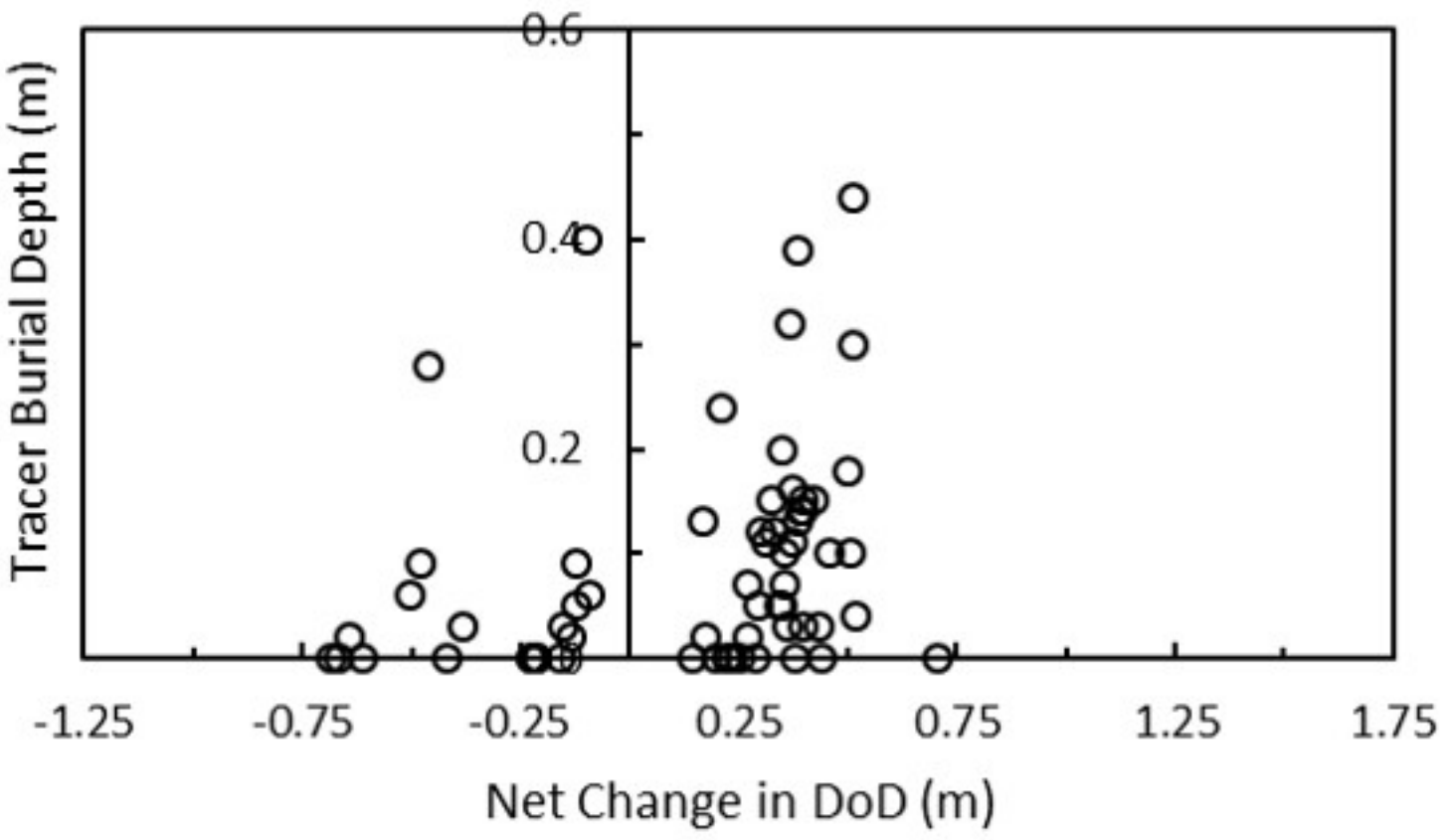

Figure 19.

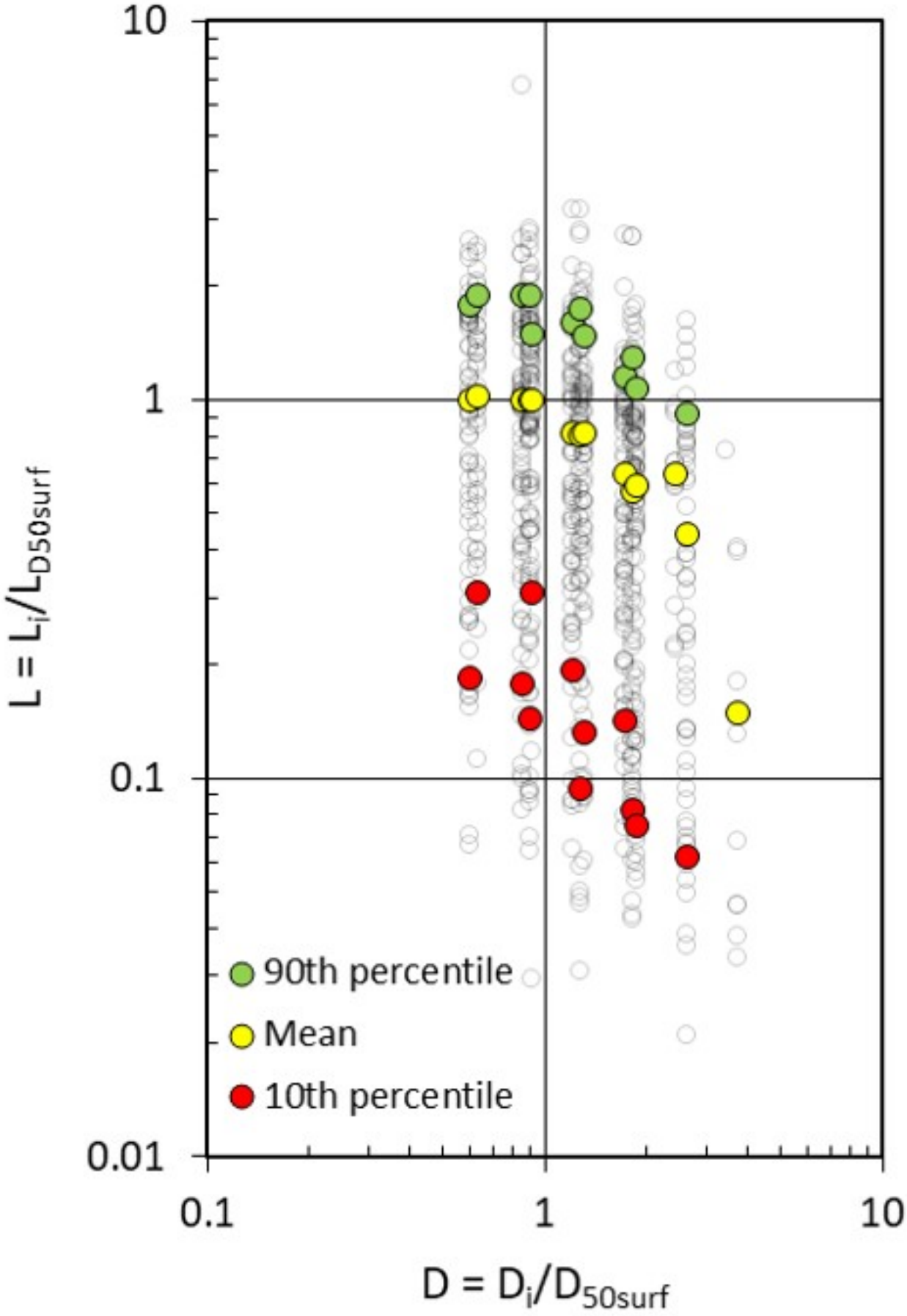
10
1
0.1
0.01
0.1
1
10
L = Li/LD50surf
D = Di/D50surf
90th percentile
Mean
10th percentile

Figure 20.

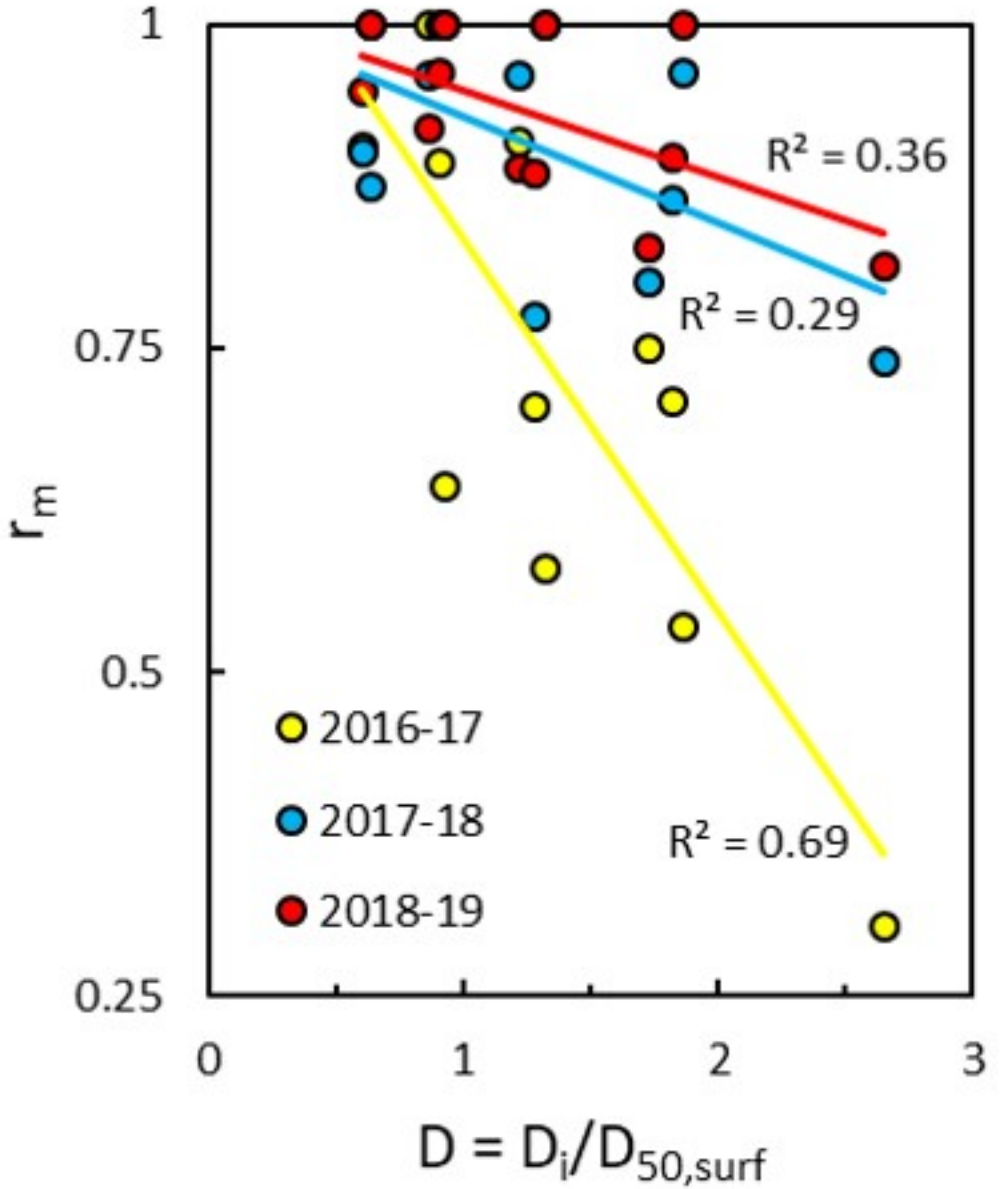
1
0.75
0.5
0.25
r_m
0
1
2
3
$D = D_i/D_{50,surf}$
$R^2 = 0.36$
$R^2 = 0.29$
$R^2 = 0.69$
2016-17
2017-18
2018-19

Figure 21.

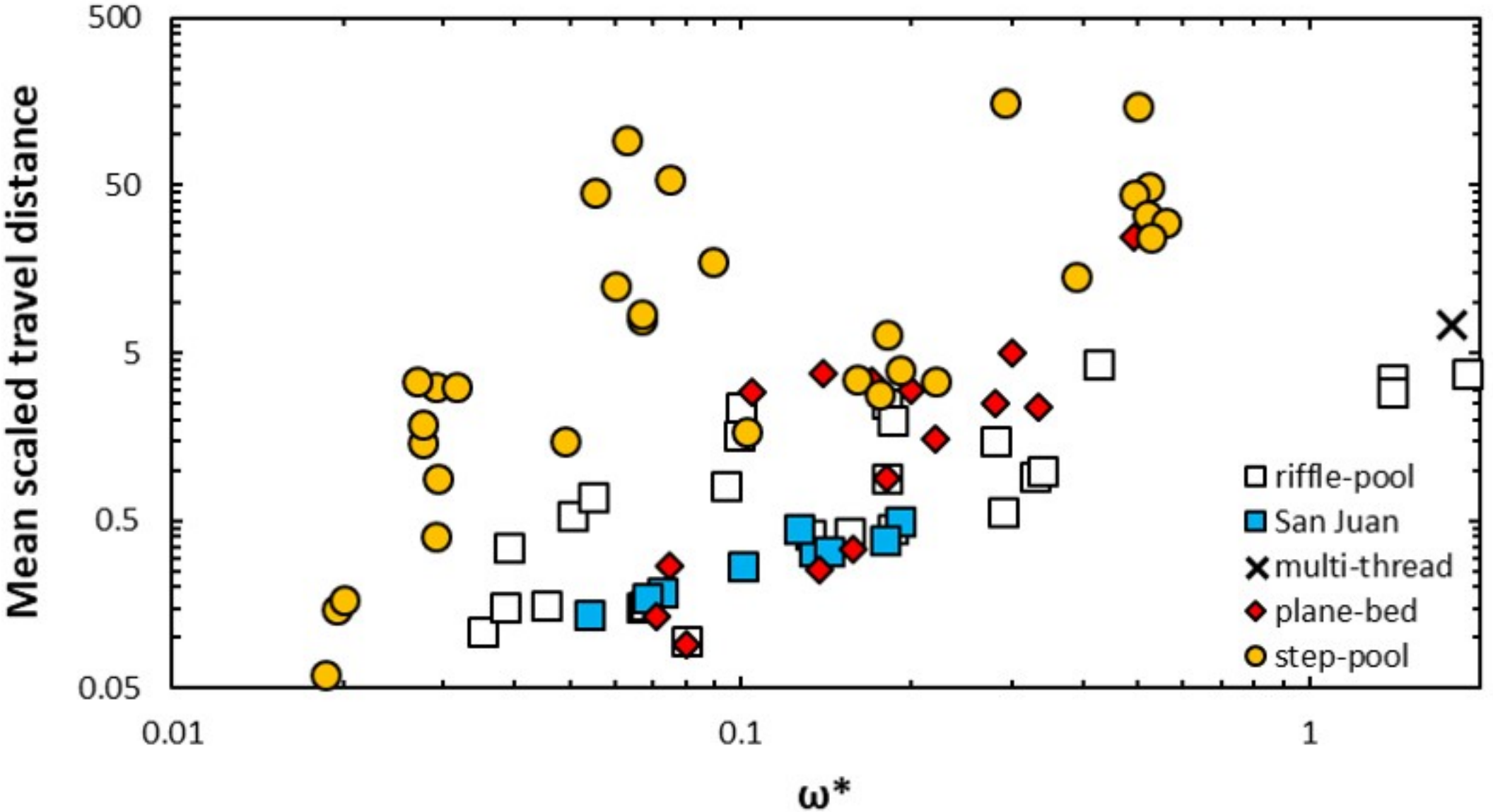
Mean scaled travel distance
500
50
5
0.5
0.05
0.01
0.1
1
ω*
riffle-pool
San Juan
multi-thread
plane-bed
step-pool

Bed particle displacements and morphological development in a wandering gravel-bed river

R. McQueen[1], P. Ashmore[2], T. Millard[1], and N. Goeller[3]

[1]British Columbia Ministry of Forests, Lands, Natural Resource Operations and Rural Development, Nanaimo, BC, Canada, [2]Department of Geography, The University of Western Ontario, London, Ontario, Canada, [3]British Columbia Ministry of Environment and Climate Change Strategy, Victoria, BC, Canada

Corresponding author: Ryan McQueen (rmcquee4@uwo.ca)

Key Points:

- Annual bed particle displacements reflect morphologic controls and differences in the annual flow regime
- Bed particle transport and burial is directly tied to patterns of bar-scale erosion and deposition
- Tracer deposition focused along bar margins, primarily at or downstream of the first downstream bar apex

Abstract

Bed particles were tracked using passive integrated transponder (PIT) tags in a wandering reach of the San Juan River, British Columbia, Canada, to assess particle movement around three major bars in the river. In-channel topographic changes were monitored through repeat LiDAR surveys during this period and used in concert with the tracer dataset to assess the relationship between particle displacements and changes in channel morphology, specifically, the development and re-working of bars. This has direct implications for virtual velocity and morphologic based estimates of bedload flux, which rely on accurate estimates of the variability and magnitude of particle path lengths over time. Tracers were deployed in the river at three separate locations in the Fall of 2015, 2016, 2017 and 2018, with recovery surveys conducted during the summer low-flow season the year after tracer deployment and multiple mobilising events. Tracers exhibited path length distributions reflective of both morphologic controls and year to year differences related to the annual flow regime. Annual tracer transport was restricted primarily to less than one riffle-pool-bar unit, even during years with a greater number of peak floods and duration of competent flow . Tracer deposition and burial was focused along bar margins, particularly at or downstream of the bar apex, reflecting the downstream migration and lateral bar accretion observed on Digital Elevation Models (DEMs) of difference. This highlights the fundamental importance of bar development and re-working underpinning bedload transport processes in bar-dominated channels.

1 Introduction

In gravel-bed rivers there is a natural feedback between channel morphology and bedload transport. The morphology of the channel is developed through the movement and deposition of individual bed particles and in turn the spatial patterns of bed material transport are controlled at least in part by the morphology of the channel (Church, 2006; Church and Ferguson, 2015). Therefore, attempts at calculating bed material transport rates, or more generally in studying bedload processes, need to consider morphologic controls on bed particle dynamics. This is particularly relevant when employing the virtual velocity approach to estimating bedload flux because it relies upon an accurate measure of the distribution and variability of particle path lengths (travel distances), which may differ greatly in channels of different morphology (Ashmore and Church, 1998; Vázquez-Tarrío et al., 2018). One idea suggested by Neill (1987), is that bed particle path lengths may be related to, and inferred directly from, the channel morphology. Depositional features such as bars are self-formed through individual particle displacements, so it follows that over the long-term the predominant particle path lengths must be related to the scale and spacing of the bars. This idea is appealing because with sufficient data tying particle path length and burial with the morphological development of bars, it may eventually allow path length to be estimated from morphology without the need for time-consuming and resource intensive direct particle tracking. However, evidence from field-based studies to support the link between bar morphology and particle path length is currently weak (Hassan and Bradley, 2017).

Throughout the bedload tracking literature, the idea that hydraulic forcing is the primary control on particle transport is prevalent, and functional relationships between average particle travel distances and the combination of flow strength and/or grain size have been developed. Hassan and Church (1992) demonstrated that mean tracer path length and excess stream power are positively correlated for single discharge events. More recently, Phillips and Jerolmack

(2014) used an impulse framework to describe the effects of flow strength on particle transport. Church and Hassan (1992) showed that there is a non-linear relationship between mean particle path length and the size of the particle scaled by the median size of local subsurface bed material, whereby travel distances of particles smaller than the median are relatively insensitive to increasing grain size, but that there is a rapid decline in path length with increasing grain size for particles larger than the median grain size of local subsurface bed material. These findings have since been re-affirmed with data from studies across a range of channel types (Hassan and Bradley, 2017; Vázquez-Tarrío et al., 2018), though data from larger, bar-dominated channels is lacking. Milan (2013) demonstrated that this effect is, at least in part, caused by differences in the duration of competent flow for different grain sizes. Many tracer studies, however, have noted differences between path length distributions and theoretical models because of tracers accumulating at distinct regions related to the river morphology (e.g. Bradley and Tucker, 2012). One example of this is the tendency of tracers to be preferentially transported to and stored in gravel bars in channels with riffle-pool-bar morphologies, especially over longer time-scales (Ferguson et al, 2002; Haschenburger, 2013).

In a literature review and re-analysis of published tracer data, Pyrce and Ashmore (2003b) found that the positively skewed path length distributions consistently reported in the literature occurred during moderate discharge events or in smaller channels lacking well-developed sedimentary structures or bar morphology. However, they found that in bar-dominated channels, high magnitude flows (i.e. those capable of altering or forming bars) lead to bi- or multi-modal distributions related to the location of bars. Pyrce and Ashmore's (2003b) flume experiments of an alternate bar channel aligned with these findings, as the authors demonstrated that during bar-forming flows most tracers were deposited on the first bar downstream from the upstream pool in which particles were seeded. Only during lower flows at the critical discharge for gravel entrainment, were positively skewed distributions, with path lengths shorter than bar spacing, observed. Using the same tracer dataset, Pyrce and Ashmore (2005) showed that during bar formation and development bed particle path lengths are commensurate with the spacing of erosion and depositional sites, and that deposition locations tied to bar development processes. In another flume experiment, Kasprak et al. (2015) demonstrated that tracer path lengths were closely related to erosional and depositional processes associated with bar development in a braided channel, with average path lengths on the scale of confluence-diffluence spacing. Similar results have been yielded from more recent modeling of braided channels (Peirce, 2017; Middleton et al., 2019). The question remains however, as to whether these observations are seen in full-scale rivers where conditions are less controlled.

In a synthesis and re-analysis of previously published field-based tracer data, Vázquez-Tarrío et al. (2018) explored the influence of both hydraulic and morphologic controls on particle transport for a range of channel types. They noted that there was a weak positive correlation between stream power and average travel distance for the dataset. However, when travel distance was scaled by a morphological length scale for each channel type (i.e. the spacing between macroscale bedforms), the scatter in the relationship was reduced, indicating that tracer transport has some dependence on channel morphology. Furthermore, analyses of empirical predictors of path length have pointed toward channel width as the most significant control on travel distance (Beechie, 2001; Vázquez-Tarrío and Batalla, 2019). For bar-dominated channels, this may imply that bar spacing exerts a control on path length because the longitudinal spacing of bars is proportional to channel width. These analyses are the starting point to investigating the relationship between path length, bar development and channel scale, but currently this lacks

tracer-based data collected in larger bar-dominated channels where morphologic control is expected to be most significant. Therefore, there remains uncertainty as to whether the principles of bed particle dynamics and statistics of displacements, derived from smaller rivers, such as step-pool, plane-bed and low amplitude pool-riffle channels (Montgomery and Buffington, 1997), are applicable to bar-dominated channels with more complex morphology and higher rates of morphological change, and further, if spatial patterns of tracer deposition and burial are tied to bar development.

The paucity of tracer data collected in larger rivers may be explained in part by logistical challenges in searching such large areas of channel, and the potentially deep burial of tracers resulting in low recovery rates. One solution that is increasingly being used to track bed particle movement in larger channels, is the use of passive integrated transponder (PIT) tags (Hassan and Bradley, 2017). PIT tags are small, glass, cylindrical capsules that operate using radio frequency identification (RFID) technology. Several factors make PIT tags an effective technology for bedload tracking including their long lifespan, resistance to abrasion and breakage (Cassel et al., 2017a), and the ability to distinguish individual particles from one another using unique codes. Furthermore, as smaller PIT tags are being developed, an increasingly wide range of sediment sizes can be tracked (Hassan and Roy, 2016). Technological improvements in PIT tag technology, such as the increased read range of antennas (Arnaud et al., 2015), innovative surveying strategies (Arnaud et al., 2017) and the development of "wobblestones" (Papangelakis et al., 2019; Cain and MacVicar, 2020), have made it more possible to track bed particle movement in larger rivers. Active ultra high frequency (a-UHF) RFID tags have also been used to explore active layer depths (Brousse et al., 2018) and particle paths (Misset et al., 2020) in wandering/braided channels, providing the benefit of larger detection ranges than PIT tags. Due to their large size however, aUHF tags can only be fit into natural particles with a b-axis of at least 70 mm or molded into synthetic pebbles (Cassel et al. 2017b; Cassel et al., 2020).

The primary objective of this study was to explore the relationship between channel morphology and particle path lengths in a large, wandering gravel bed river – the San Juan River, British Columbia, Canada. Wandering channels are irregularly sinuous and can display aspects of both meandering and braided channels. These channels are characterized by complex bar development and some degree of lateral instability (O'Connor et al., 2003; Beechie et al. 2006). Typically, the most common bar morphology is a lateral bar and the dominant mode of deposition is lateral bar accretion (Desloges and Church, 1987; Rice et al., 2009). Church and Rice (2009) describe a pattern of bar evolution whereby vertical growth is limited by the height at which sediment can be elevated, and the longitudinal growth of bars is limited by the length-scale of the channel, resulting in bars primarily growing laterally. This pattern of rapid lateral accretion may persist for decades (Rice et al., 2009) and is accompanied by the erosion of the opposite bank, producing a laterally unstable channel with less systematic migration than true meandering channels (McLean et al., 1999; Fuller et al., 2003). We expect this pattern of bar and channel evolution to be reflected in spatial patterns of tracer displacements for the San Juan River, as bars are by definition an expression of the displacement, transport and deposition of individual bed particles. If path lengths are tied to morphology in bar-dominated channels, then particle displacements and burial should be tied to patterns of morphological change over a defined period. To address this objective, PIT tags were used to track bed particle movements and repeat LiDAR surveys were conducted to measure topographic change and bar development during the tracer monitoring period. Combining tracers with topographic change captured at high resolution is uncommon in the literature and allows a more comprehensive interpretation of the

process-form coupling of bedload transport and channel morphology than can be achieved via either method separately (Vericat et al., 2017).

2 Materials and Methods

2.1 Study Site

The San Juan River, also known by its First Nation name, the Pacheedaht, is located on southern Vancouver Island, British Columbia and drains an area of about 730 km^2 (Figure 1a). The main channel is over 50 km long with a total relief of 690 m. The San Juan River valley follows a major east-west fault with distinct topography and bedrock geology on the north and south sides. Bedrock north of the river consists of a series of volcanic and intrusive units, whereas the south side of the valley is underlain almost exclusively by metamorphic rocks of the Leech River Complex (BCGS, 2019). The river outlets to the Strait of Juan de Fuca, near the town of Port Renfrew (Figure 1a).

Forest harvesting in the San Juan River Watershed dates back to the early 1900s and has been linked to changes in physical habitat and channel morphology in the mainstem and tributaries (NHC Ltd., 1994). This study was guided by watershed management objectives, to provide detailed information on the current sediment dynamics and morphologic changes in the San Juan River which will help inform future restoration decision making.

The study focused on the lower alluvial reach of the San Juan River beginning near Red Creek, downstream of a canyon reach (Figure 1b). The alluvial channel exhibits a wandering morphology, as defined by Mollard (1973) and Neill (1973), with an active width varying between 50-150 m and a reach-averaged slope of 0.0011 m m^{-1}. During low-flows the river has a single identifiable main channel though it displays a multi-channel pattern during higher-flows when secondary channels are active. Riffle-pool-bar sequences are the primary macroscale bedforms in the alluvial reach, with bars typically on the order of several hundred metres long and up to 100 m wide. Bars are composed primarily of gravel, cobble and sand and there is a general trend of downstream fining of surface sediment calibre both within and between bars. For referencing purposes, mainstem bars were numbered, with Bar 1 being the farthest upstream and subsequent bars numbered in ascending order downstream. Particle tracking focused on Bars 6, 7 and 15, the most accessible sites along the river (Figure 1b). These bars are representative of the typical length and width, overall appearance, and grain sizes found in the alluvial reach. The morphology of the study bars is summarized in Table 1.

The closest gauging station to the study sites is the Water Survey of Canada hydrometric station 08HA010, which is installed on the lower San Juan River, approximately 2.5 km downstream from Bar 15 and 7.5 km from Bar 6 (Figure 1b). The 2-, 10-, and 100-year floods are approximately 800, 1050 and 1200 $m^3 s^{-1}$ respectively, though the upper end of the rating curve is uncertain due to the difficulty of obtaining discharge measurements during peak floods (Figure 2). Mean monthly discharge varies from a high of 97 $m^3 s^{-1}$ in January to a low of 4.5 $m^3 s^{-1}$ in August, with a mean annual discharge of 49 m^3/s (WSC, 2019). The discharge regime closely follows the seasonal trend in rainfall because 99 % of annual precipitation at low elevations falls as rain (ECCC, 2019), with only transient snow accumulations (no seasonal snowpack) at higher elevations within the watershed.

194 2.2 Tracer stone deployment and tracking

195 Half duplex low-frequency (134.2 kHz) PIT tags were inserted into individual gravel bed
196 particles to track annual particle movements around three major bars in the San Juan River. Low-
197 frequency tags are ideal for tracking in coastal and fluvial environments because their signal can
198 pass through water and can penetrate most non-metallic objects (sediment, wood, etc.) better
199 than high and ultra-high frequency tags (Chapuis et al., 2014; Schneider et al., 2010). In 2015,
200 100 tracers were installed along a cross-section at the head of Bar 6, while between 2016-2018 a
201 further 1199 tracers were installed across the three study sites (Bars 6, 7, and 15) with between
202 125-142 tracers per site annually. A combination of 12, 23, and 32 mm long PIT tags were used
203 in the original 2015 deployment. However, by 2017 only the 32 mm tags were used because of
204 their larger read range (Chapuis et al., 2014) and higher recovery rates during the first recovery
205 survey.

206 Wolman particle size counts were conducted at each site to characterize the size
207 distribution of surficial bed material (Table 2) (Wolman, 1954). Native stones were then
208 collected from the San Juan River and brought back to the lab for preparation, which included
209 drilling a cavity in each particle, inserting and epoxying an RFID tag in place, and painting the
210 stone (similar to methods to described in Eaton et al., 2008). Particles were selectively chosen to
211 reflect the size distribution of bed surface material in the channel as best as possible (Figure 3).
212 However, PIT tags did not fit into particles smaller than 22 mm, thus the fine end of the bed
213 material distribution was not well represented. Differences between the size distribution of bed
214 material and tracers was greatest for Bar 15, which had the finest material of the three study bars
215 (Table 2). However, the Bar 15 tracer distribution does reflect well the size distribution of local
216 surface bed material greater than 22 mm (Figure 3c). The use of 32 mm tags in 22-32 mm tracers
217 biased this size class towards particles with an a-axis longer than 35 mm.

218 Tracers were deployed annually in the fall, prior to winter flooding, along launch lines
219 perpendicular to the direction of flow. Each launch line spanned the bar head, riffle, and tail of
220 the opposite (upstream) bar, providing the opportunity to observe tracer dispersion around major
221 bars, and to observe differences in particle mobility and path lengths across different
222 morphologic units. While particle path lengths are unlikely to be influenced by seeding position
223 across the channel cross-section in smaller, plane-bed type streams, it has been shown to play a
224 significant role in particle movement in riffle-pool channels with well-developed bar
225 morphology (Liébault et al., 2012). Clusters of tracers were deployed at one to two metre
226 intervals along the launch line by replacing particles on the surface of the riverbed with tracer
227 stones to mimic natural positions and local bed texture. Tracers starting on the surface of the
228 riverbed are more exposed to flow than buried or locked particles, and therefore, observed travel
229 distances in this study are likely to be over-estimates of annual transport distances for the bed as
230 a whole.

231 Tracer recovery surveys were conducted annually during the low-flow seasons at the end
232 of July through August for 2016 to 2019. All recovered tracers were removed from the channel
233 and redeployed at their original launch line the following fall so that each year the deployment
234 strategy was a repeat of the previous one. The winter storm season with several mobilizing flows
235 is treated as an annual event producing annual particle displacements in relation to morphology.
236 This allowed us to assess the morphologic influence on tracer displacements through repeat tests.
237 This decision was also influenced by the practicalities of tracking sediment in a large river
238 because tracking after every event would be onerous and leaving tracers in the channel would

likely necessitate increasing the downstream extent surveyed every year, which would quickly become untenable in a river of this size. Furthermore, excavating and removing tracers from the channel allowed us to directly measure tracer burial depths which provides valuable information on active layer dimensions and gives context to particle deposition in relation to morphological development. The maximum downstream extent of survey differed for each location, though generally the first two bars downstream of each seeding site were searched. The deepest portions of pools were omitted from the searching process because they were not wadable, even at low-flow.

Two antennas were used to search for tracer stones. A small handheld wand antenna, the 'BP Plus Portable', and a larger 'Cord Antenna System', both were purchased from BioMark® (Figure 4). Based on testing in the lab, the wand antenna had a maximum read range around 40-50 cm for the 32 mm PIT tags, though the tag signals are anisotropic, and the read range was as low as 10 cm for certain orientations. The wand antenna was used as the sole antenna for tracer recovery in 2016, resulting in a low recovery rate (33 %), and was used only as a supplementary tool to the larger antenna for subsequent years. Since PIT tag signals interfere with one another when in close proximity (Lamarre et al., 2005; Chapuis et al. 2014), the wand antenna was still a useful tool for distinguishing between PIT tags in areas where tracers were densely concentrated - typically the launch line, as a fraction of the tracer population remained immobile. The wand antenna was also effective for refining the position of tracers after detection with the cord antenna.

The cord antenna system consisted of the cord antenna cable, secured to a 15' x 5' (5 m x 1.5 m) rectangular PVC pipe frame, mounted to a backpack frame using a series of ropes, pulleys and cams (Figure 4b). The frame held the cable in a (semi-) rigid structure, stabilising the antenna and allowing it to keep a high current. The operator stood in the centre of the rectangle wearing the backpack and could manipulate the height of each corner of the antenna to help navigate obstacles and changing topography in the field (Figure 4b). The cord antenna covered a much larger surface area than the wand antenna, making it an ideal tool for searching large areas efficiently. It also had a much larger range of detection than the wand antenna, with a maximum read range around 1.75 m, and thus could detect tracer stones buried at greater depths.

Once detected, tracer positions were recorded using one of two methods, and dug up (where possible) to determine a burial depth. For tracers that moved only a short distance (less than 20 m or so), a measuring tape was used to directly measure transport distances from the launch line. For tracers moving larger distances, a handheld Garmin GPS unit was used to record tracer locations. GPS waypoint errors were on the order of two to three metres, which was considered acceptable for the purpose of determining typical particle path lengths, since average path lengths were generally around 100 m, resulting in less than five percent error.

2.3 Geomorphic change detection

2.3.1 Topographic surveying

In addition to particle tracking, repeat aerial LiDAR surveys, flown by Terra Remote Sensing Inc. in 2015, 2018, and 2019, were contracted for the study and other projects related to management of the river. Each LiDAR survey was conducted using the Reigl LMS-1780 sensor from an airborne platform. Ground accuracy tests, performed by Terra Remote Sensing Inc., involved both internal and external horizontal and vertical checks (TRS Inc., 2018a,b, 2019).

Internal checks were conducted via comparison of intra- and inter-flight areas of overlap. External checks consisted of two components: comparison of the LiDAR ground surface with control stations not used in the calibration process, and with a series of check points collected on open surfaces using Post Processed Kinematic (PPK) GPS. A root mean square error for vertical precision ($RMSE_v$) of less than ten centimeters was reported for all surveys (Table 3) (TRS Inc., 208a,b, 2019). Survey point densities were spatially variable across the study sites. Average point densities ranged from 12 to 38 points per square meter with differences based largely on ground cover and topography (Table 3). LiDAR point clouds were filtered by ground and non-ground classes by Terra Remote Sensing Inc. (TRS Inc., 2018a,b, 2019). LiDAR point clouds were used to generate a series of raster-based digital elevation models (DEMs) of the study sites. LiDAR DEMs were produced for each survey at a 10 cm spatial resolution by converting point clouds to a Trinagulated Irregular Network (TIN), from which concurrent raster DEMs were generated using linear interpolation. Topographic changes between survey dates were then calculated by processing the LiDAR DEMs using the Geomorphic Change Detection (GCD) software (Wheaton et al., 2010) to produce DEMs of difference (DoDs). In-channel areas that were inundated in both the old and new DEMs, where point cloud returns were either non-existent or affected by refraction were not used in building DEMs, restricting change detection analysis to above-water areas. To capture bank erosion, a minimum level of detection of one metre was used in change detection analysis for areas that were wet in the new DEM but were vegetated banks in the old DEM. This threshold allowed us to observe changes in bank position, as the riverbanks are two metres or taller throughout the alluvial reach.

The LiDAR-derived DoDs (Difference of DEMs between successive surveys) were used to interpret patterns of tracer displacement and burial depths, and to provide information on morphological development of the bars during the study period. They were not used to calculate complete reach-scale sediment budgets due to the lack of in-channel topographic data and stage differences during each LiDAR survey affecting the relative portion of the river bed that was exposed. Currently, collecting reach-scale bathymetric data in large channels is challenging and relies on either boat-based multibeam echo sounding (MBES) systems or green wavelength LiDAR sensors (Tomsett and Leyland, 2019).

2.3.2 DEM analysis

To account for uncertainty in the DEMs, a spatially variable uncertainty analysis was conducted using the GCD ArcMap extension. This involves three main steps: 1) an estimate of uncertainty for each individual DEM; 2) propagation of these errors through the DoD; and 3) an assessment of the statistical significance of these uncertainties in distinguishing real geomorphic change from noise (Wheaton et al., 2010). A major appeal of this method is that it requires little to no additional survey error information other than the survey data itself. Further, accounting for spatially-variable error allows for recovery of information in areas with low elevation uncertainties that would otherwise be lost.

For each DEM, two surfaces were generated for uncertainty analysis using the built-in tools in the GCD software: a point density raster and a slope raster. The rationale behind using these surfaces was that steep areas with low point density have high elevation uncertainty, whereas flat areas with high survey point density will generally have lower elevation uncertainty (Wheaton et al., 2010). These surfaces were then combined on a cell-by-cell basis, using a fuzzy inference system (FIS), to produce an elevation uncertainty surface. Uncertainty surfaces

associated with individual DEMs were then combined using simple error propagation (Brasington et al., 2003) to produce a single propagated error surface for the DoD. The GCD software then uses probabilistic thresholding to determine the statistical significance of these uncertainties. The probability that the elevation change associated with each individual cell of the DoD is then assessed at a user-defined confidence interval, in this case 80 %. Originally, 95 % was chosen, however upon examination of output thresholded DoDs, this limit appeared too restrictive, with real change being removed from areas of eroding banks and in obvious areas of deposition.

2.4 Hydrological Analysis

Discharge data from the WSC hydrometric station were used to characterize differences in the hydrologic conditions between study years. A bankfull discharge (Q_{bf}) of 500 $m^3 s^{-1}$ was visually estimated from time-lapse imagery, roughly the one year return interval flood (Figure 5), with Q_{bf} being defined as the discharge at which the entire active width of the channel was inundated. This was used as a reference discharge to approximate the number of mobilising flow events per year. While previous research indicates that flows less than bankfull may mobilise coarse bed sediment (Ryan et al., 2002; Pfeiffer et al., 2017; Phillips and Jerolmack, 2019), a threshold discharge for gravel entrainment could not be accurately established for this study because tracers were exposed to multiple potentially mobilising events each year, rendering it impossible to determine which specific events caused tracer movement. Further, the complexity of channel morphology and variability in tracer grain size makes a single threshold discharge difficult to define for this study. Despite this, Q_{bf} still provides a relative basis for the number of potential mobilising flows, and the hydrograph for the period of the tracer study illustrates that even if the reference discharge were shifted substantially, say 100 $m^3 s^{-1}$, the number of mobilising events would change very little (Figure 6).

Previous tracer studies have used the total excess flow energy (Ω_T) as a metric to capture the intensity and duration of competent flow for multiple flood events (Haschenburger, 2013; Papangelakis and Hassan, 2016). However, this requires knowledge of the critical discharge, which was unknown for this study. Instead, a modified Ω_T was used in analysis for this study, whereby the total flow above estimated bankfull was integrated over the period between tracer deployment (t_d) and recovery (t_r):

$$\Omega_T = \rho g S \int_{t_d}^{t_r} (Q - Q_{bf}) dt$$

where ρ is the density of water (1,000 kg m^{-3}), g is the acceleration due to gravity (9.81 m s^{-2}), and S is the reach-average slope. Discharge data was integrated at five minute intervals (as collected at the WSC hydrometric station). The modified Ω_T, along with annual peak instantaneous discharge (Q_{max}), and number of potentially mobilising events ($Q>Q_{bf}$) were recorded for each study year to give context to differences in tracer mobility, path lengths, and burial data that might be the result of different hydrologic conditions between years. The primary purpose of this analysis is to identify any differences in annual path lengths that can be attributed to differences in the annual flow regime, and to then compare any observed differences with morphologic constraints on path lengths that may occur over the longer term related to, for example, deposition on bars.

3 Results

Tracer recovery rates were generally high for a river of the size and scale of the San Juan River (see Table 1 in Chapuis et al., 2015), with annual recovery rates exceeding 65 % for all but one of the deployments (Table 4). The low recovery rate (33%) of tracers from the original 2015 deployment was a result of the surveying approach used in searching for tracers, as only the smaller handheld wand antenna was used in the initial recovery survey in 2016. The low recovery rate from this deployment limited interpretation and analysis of the data from this year, and as such was removed from analyses presented in this section unless specifically noted.

3.1 Discharge effects on particle dynamics

A total of 21 events with peaks greater than 500 $m^3 s^{-1}$ occurred from 2015 to 2019, ranging from four to six events per study year (Table 4). The annual instantaneous Q_{max} during the tracer study ranged from 749 $m^3 s^{-1}$ (2016-17) to 1,022 $m^3 s^{-1}$ (2015-16) corresponding to roughly 2-yr and 6-yr return interval floods (Table 4; Figure 2). Using the modified Ω_T as a metric, the 'wettest' year (i.e. greatest amount of flow exceeding Q_{bf}) was 2017-18, the 'driest' year was 2016-17, while 2015-16 and 2018-19 had Ω_T values in between (Table 4). The sensitivity of Ω_T to the defined Q_{bf} was tested, and shifting Q_{bf} to 400 $m^3 s^{-1}$ or 600 $m^3 s^{-1}$ made no difference to the relative ranking of Ω_T between study years, and made little difference to proportional differences between years.

To assess annual differences in tracer movement related to discharge, Ω_T was plotted against the mobility rate, median path length, and mean burial depth for each site and study year (Figure 7). The relative mobility of tracers (r_m) appeared insensitive to differences in Ω_T. For each bar, more than 80 % of tracers were mobilized each year, with the exception of 2016-17 Bar 15 tracers (48 % mobile) (Figure 7a). The low mobility of these tracers relative to other deployments may be a result of both low Ω_T and also local morphodynamics (see section 3.3).

The median path length of tracers (L_{50}), scaled by the local bar length, showed a general positive relationship with Ω_T, though this was not statistically significant when pooling the data between sites ($R^2 < 0.05$) (Figure 7b). Tracers seeded at each bar tended to show different responses to increasing Ω_T. The influence of Ω_T on Bar 6 and Bar 7 tracers was unclear, as the wettest year of the study, 2017-18, did not produce the highest L_{50} for either site (both had greater L_{50}'s in 2018-19). However, the path length of Bar 15 tracers sharply increased with Ω_T for the three years of study (Figure 7b). Despite any increases in annual path length associated with Ω_T, most tracers were limited to transport distances less than one bar-length. This implies that any longer-term morphologic constraints on path length, such as deposition within bars, is unlikely to be substantially affected by differences in the typical annual flow regime. However, this may not hold true for extreme events capable of major morphologic change in the bars and river morphology.

Overall, there was an increase in burial depth with increasing Ω_T when pooling the data across all sites ($R^2 = 0.49$) (Figure 7c). The largest deviation from the general linear trend was the 2018-19 deployment of tracers at Bar 6 (B_{avg} = 20 cm). Bar 15 exhibited the lowest average burial depths, while Bar 6 and 7 tracers were typically buried deeper (Figure 7c). Tracer burial is explored in more detail in section 3.3 with respect to topographic changes observed on DoDs.

Path length frequency distributions for tracers deployed at Bars 6, 7, and 15 are presented in Figure 8 and maps illustrating the final position of recovered tracers are presented in Figures 9, 10, and 11 respectively. The path length distributions for 2016-17, the 'driest' year, were positively skewed for all three sites (Figure 8) with the lowest median path lengths (L_{50}) of any of the years of study (Table 4). The following year, 2017-2018, was the 'wettest' of the study period. The Bar 6 path length distribution was also positively skewed this year, though the L_{50} increased from 69 m to 130 m downstream reflective of the increased hydrologic conditions (Table 4). The 2017-18 Bar 7 and Bar 15 path length distributions followed roughly symmetrical distributions, with the primary mode of tracer deposition occurring at the bend apex next to Bar 7 (Figure 10b), and just downstream of the apex at Bar 15 (Figure 11b). In 2018-19, the year with moderate Ω_T, Bar 6 tracers exhibited a bi-modal distribution with the primary mode of deposition occurring just upstream of the bend apex and a secondary mode reflecting short-transport distances (Figure 9b). Bar 7 and Bar 15 path length distributions for 2018-19 were positively skewed, though there was a minor peak in the Bar 7 distribution, reflecting tracers accumulating on the bar tail (Figure 8b, 10c). Overall, the shape of path length distributions generally reflected discharge conditions, whereby positively skewed distributions were observed for the driest year, bi-modal distributions were observed for two of the three sites for intermediate hydrologic conditions, and roughly symmetrical distributions, centered around the bend apex at each bar were observed for two of the three sites during the wettest year.

3.2 Morphologic effects on particle displacements

Tracer path lengths were scaled by the length of the bar at which they were seeded to better compare particle displacements between the three bars (Figure 12). The distribution of scaled path lengths were significantly different (Kruskall-Wallis test, $p<0.05$) among all three sites whereby Bar 6, Bar 7 and Bar 15 had median scaled path lengths (L_{50}) of 0.20, 0.34 and 0.41 'bar-lengths' respectively (Table 5). Bar 6 tracers, while having the highest mobility rate (89 % mobilised), had the lowest L_{50}, with 90 % of tracers depositing upstream of the bar apex (which is at approximately $L = 0.50$) (Figures 9 and 12). For both 2016 and 2018 Bar 6 deployments, there was a clustering of tracers just upstream of the bend apex that appears to be related to the growth of a coarse gravel sheet with a slip face roughly one metre high, which migrated downstream from the bar head between 2015 and 2019 (Figure 13). While transport past the apex was more common for Bars 7 and 15, these tracers still tended to be deposited within the initial bar in which they were seeded, with deposition focused along bar margins (Figures 10 and 11). This is also highlighted by the tracer escape rates, that is the fraction of mobile tracers recovered downstream of the initial bar in which they were seeded. Less than one percent of tracers escaped Bar 6 annually, five percent escaped Bar 7, and four percent escaped Bar 15 (Table 5) indicating that annual particle displacements on the San Juan River tend to be within one riffle-pool-bar unit.

Tracers recovered in the wetted channel, closer to the thalweg, may be more likely to be remobilised by future events, and as such represent potential future frontrunners, while those stored on gravel bars are less likely to be remobilized, and may become trapped in the bars with future transport limited by bar development and re-working. For Bar 6, 66 % of tracers were deposited in or on bars, while 34 % were recovered in the wetted channel. Similarly, 71 % of Bar 7 tracers were recovered on bars versus 29 % in the wetted channel. Bar 15 appears to trap less sediment than the other sites, as only 46 % of tracers were recovered on gravel bars versus 54 % in the wetted channel, as Bar 15 is less-developed laterally than the other study bars. For each of

the sites however, the proportion of tracers recovered on gravel bars reflects more than just those transported to and deposited on bars, it also reflects tracers that were originally seeded on bar tails and remained there. The role of initial seeding morphology was explored by partitioning the data by the morphologic unit in which tracers were originally deployed (Table 6). The Bar 6 2016 launch was treated separately from the rest of the Bar 6 data as the launch line was located 120 m downstream of the other years, with tracers seeded across the bar edge and adjacent pool. In general, tracers seeded on bar tails tended to have lower relative mobility than those seeded on the bar heads or in the wetted channel (Table 6). The exception to this was that 80 % of bar tail tracers were mobilised for Bar 15 versus 73 % mobility in the wetted channel (Table 6). When breaking this data down further however, 92 and 93 % of wetted channel tracers were mobilized at Bar 15 during 2017 and 2018 deployments respectively, and only the 2016 tracers exhibited low mobility in the wetted channel (40 % mobile). Tracers deployed on bar heads were almost always mobilized (100 % mobile for Bar 6, and 98 % for Bar 15), suggesting that these areas are active erosional sites. These differences highlight the importance that deployment strategy and channel morphology can have on tracer dispersion, as recently shown by McDowell and Hassan (2020).

Box plots of tracer scaled path lengths for each seeding morphologic unit for each study site is presented in Figure 14. For Bar 6 (2015, 2017, 2018 deployments), tracers seeded on the bar tail had a lower median scaled path length than those seeded on the bar head or in the wetted channel (Table 6). However, differences in the distributions between seeding morphologies was not statistically significant (Kruskall Wallis test, $p > 0.05$). Bar 6 tracers tended to be deposited upstream of the bar apex regardless of where they were initially seeded, with clustering coincident with the development of the migrating gravel sheet terminating at the bar apex (Figure 13). For the 2016 Bar 6 deployment, there was a statistically significant difference (Mann Whitney U test, $p<0.001$) between the path length distribution of tracers seeded in the wetted channel (specifically a pool in this case) and those seeded on the bar edge. Bar edge tracers were restricted to path lengths less than 0.3 bar lengths downstream, while those seeded in the pool more frequently travelled farther downstream, with a maximum observed path length of 0.78 bar lengths (Table 6). Again, bar edge tracers appear to become incorporated into the migrating gravel sheet at this location. The scaled path length distributions were significantly different (Mann Whitney U test, $p<0.001$) for Bar 7 tracers seeded in the wetted channel relative to those seeded on the adjacent bar tail, with median path lengths of 0.39 and 0.21 bar lengths for wetted channel and bar tail tracers respectively. Similarly, Bar 15 tracers seeded on the bar tail had a significantly different path length distribution than either those seeded on the bar head ($p<0.001$) or bar tail ($p<0.05$) based on a Kruskall Wallis test and Dunn's post hoc comparison. Overall, tracers seeded on bar tails tended to be both less mobile and were displaced shorter distances on average than those seeded either in the wetted channel or on bar heads, underlining the spatially variable nature of bed-material transport in bar-dominated channels.

In summary, the results indicate that particle dynamics are directly tied to the local channel morphology. Median tracer path lengths were consistently focused upstream of the bar apex of the first downstream bar, and less than five percent of tracers escaped the first downstream bar after one year of transport. Furthermore, Bar 6 and Bar 7 tracers were preferentially deposited on the bars relative to the wetted channel, with clustering along bar margins and near the bar apex region. Bar 15 tracers were more evenly split between the wetted channel and bar surfaces. In addition to this, differences were observed between the dynamics of tracers installed in different morphologic units. Those installed on bar tails were less likely to be

entrained than those beginning in the wetted channel or on bar heads, and had shorter median path lengths.

3.3 Morphologic change and particle burial

Path length data demonstrated a relation with channel morphology which can be further explored in relation to the geomorphic change detection analysis and by incorporating tracer burial depth data. DoDs are presented for 2015-2018 and 2018-2019 for the Bars 6-7 reach in Figure 15 with tracer burial depths and locations overlaid on top. Bar 15 DoDs with buried tracers for the same periods are presented in Figure 16. Tracers that were located using the cord antenna system but were too deep to be detected by the wand antenna (or physically recovered), were estimated to be deeper than 30 cm (a conservative estimate of the maximum detection range of the wand antenna). Tracers recovered in pools were not physically recovered so burial depth was unknown and they were not included in burial depth analyses.

For the Bar 6-7 reach, a general pattern of downstream bar and bend migration was observed over the period of study. More than 80 % of bar surface area was net depositional for both the 2015-18 and 2018-19 DoDs for Bar 6 and Bar 7, with average values of 0.4 – 0.6 m of net vertical deposition (Table 7). On Bar 6 the greatest magnitude of net deposition (1.7 - 2.1 m) occurred at the downstream end of advancing gravel sheet near the bar apex (Figure 13; Table 7). The greatest net erosion on Bar 6 occurred in two locations: erosion of the inner bank near the bar head (2015-18), and pools scoured at the bar tail just upstream of a bedrock outcrop (2018-19) (Table 7). For Bar 7 a similar pattern occurred with maximum net deposition observed near the bar apex (~ 1.1 m of vertical deposition) and maximum net erosion focused at the inner bank near the bar head (Table 7). In addition to the changes occurring on bar surfaces, the banks opposite of Bar 6 and Bar 7 retreated over the study period, though the magnitude of bank erosion was greatest opposite of Bar 6. In summary, from 2015 to 2019 there was a pattern of lateral bar accretion and downstream bar migration coupled with bank erosion.

The Bar 15 DoDs exhibited a similar pattern of topographic change to the Bar 6 and Bar 7 reach. Overall, the surface area of Bar 15 was net depositional for both the 2015-18 and 2018-19 DoDs with average net vertical deposition of 0.3 – 0.4 m (Table 7). The greatest magnitude of net deposition recorded on the surface of Bar 15 (~ 1.6 m) occurred mid-way down the bar and appears associated with a large fallen tree residing in the area (Table 7). The maximum net erosion on Bar 15 focused on the inner bank near the bar head (Table 7), and bank retreat was observed opposite the downstream portion of Bars 15 and 16 (Figure 16), leading to a pattern of downstream bar and bend migration.

The distribution of tracer burial depths for Bar 6, 7 and 15 are presented in Figure 17. The maximum burial depth for Bar 6 tracers was 52 cm, although 34 % of tracers were not physically recovered, and we suspect that they are buried deeper than 30 cm (because they were not detected with the wand antenna) (Figure 17a). Assuming that these tracers were buried beyond this depth, the median burial depth for Bar 6 tracers was 25 cm. A maximum burial depth of 47 cm was recorded for Bar 7 tracers, with 30 % of tracers not physically recovered, likely due to deep burial, resulting in an overall median burial depth of 18 cm (Figure 17b). For both locations, more than 40 % of tracers were recovered at depths exceeding the commonly quoted assumed active layer depth of ~2 D_{90} of the surface (Wilcock and McArdell, 1997; Hassan and Bradley, 2017). Tracer burial data from Bars 6 and 7 suggests that maximum active layer thickness may be 50 cm or greater locally. This indicates that in this type of channel the particle

exchange during bed material transport may operate at depths beyond a surface layer a few grains thick for at least a portion of the bed and active layer depth is governed by the distribution of bar-scale erosion and deposition. The median burial depth of 10 cm for Bar 15 tracers was the lowest of the three study sites (Figure 17c). The lower tracer burial on Bar 15 relative to the other sites aligns with the lower magnitudes of topographic change observed on DoDs relative to the Bar 6 and Bar 7 reach. Because morphologic change drives burial depth, and local bar dynamics and morphology differ between sites, this produces differences in tracer dispersion and burial between sites.

In general, the spatial pattern of tracer deposition was well-reflected in the DoDs. For Bar 6, 49 % of tracers were recovered in areas corresponding to known geomorphic change on the DoDs (Table 8). Of these tracers 88 % resided in depositional cells and 12 % in erosional cells. The deepest buried tracers (> 30 cm) tended to be deposited near the apex of Bar 6, which aligns with the downstream extent of the migrating gravel sheet in this area (Figure 13). For Bar 7, 65 % of recovered tracers were located in areas of known geomorphic change, with 91 % in depositional cells and 9 % in erosional cells (Table 8). The deepest buried Bar 7 tracers were recovered either near the bar apex or on the bar at the launch line (Figure 15). Due to the lack of topographic data captured in the wetted channel, only 23 % of tracers from Bar 15 were recovered in areas of known geomorphic change, in large part due the high proportion of Bar 15 tracers that remained in the initial riffle in which they were seeded. For those located in areas of known change, 70 % were located in depositional cells and 30 % in erosional cells (Table 8). Across all three study sites, tracers tended to be recovered in areas of deposition on DoDs when there was known geomorphic change, which supports the idea that particle transport and deposition is tied to overall channel morphodynamics. For the portion of tracers recovered in areas of indeterminate change on DoDs the link between particle deposition and topographic change cannot be established. However, these areas were most commonly bar margins and riffles (Figure 15 and 16), areas that are likely to be depositional environments.

There was no correlation observed between tracer burial depth and the corresponding elevation change from DoDs for any of the three sites (Figure 18). This is perhaps not surprising since the timing between tracer deployments and recoveries does not match the time between topographic surveys used to produce the DoDs and because tracers could only be recovered within approximately 50 cm of the bed surface whereas scour and fill occurred at depths beyond this (Table 7). Overall, the mean burial depth of tracers recovered in depositional cells was greater than those in recovered in erosional cells for each site, though the low number of tracers recovered in erosional cells prevents the results from being statistically significant (Table 8).

In summary, the results indicate that individual particle deposition and burial is related to the spatial pattern of bar development and re-working. Bars were net depositional over the study period, with lateral bar accretion and downstream bar migration observed for each site. Tracers were preferentially deposited in net depositional areas on DoDs relative to erosional areas, at average depths close to or exceeding twice the local D_{90}. This evidence suggests that particle exchange in this type of river operates at depths beyond a thin bed surface layer.

3.4 Grain size effects on tracer mobility and path length

The path length of San Juan River tracers exhibited a similar relationship with grain size as described previously in the literature (Church and Hassan, 1992; Hassan and Bradley, 2017), with particles larger than the local D_{50} exhibiting a steep decline in mean path length with

increasing grain size, and particles smaller than the local D_{50} showing less variation in mean path length with increasing grain size (Figure 19). However, while the mean travel distance of each tracer size fraction follow this non-linear trend, there is a large amount of scatter in the data suggesting that other factors, such as channel morphology and hydrologic conditions, play an important role on particle transport. The relative mobility of each tracer size fraction is presented in Figure 20, where the tracer size class is scaled by the local surface D_{50}. In general, relative mobility decreased with increasing relative grain size. This trend was moderately strong for the 2016-17 tracer displacements ($R^2 = 0.69$) and weak for the 2017-18 and 2018-19 displacements ($R^2 = 0.29$ and 0.36 respectively). The 2016-17 season was the 'driest' year during the study period, in terms of both Q_{max} and the total duration of competent flow, suggesting that hydrologic conditions limited mobility of larger sizes compared to the 'wetter' years when most of the bed was mobilised regardless of grain size.

4 Discussion

The results from particle tracking in the San Juan River reveal insights into bed particle dynamics in a wandering-style gravel-bed river, which has seldom been a focus in previous studies. The recovery rate of tracers in this study combined with topographic change data is unique for a channel of this size and as such provides important information on the nature of bedload transport in these systems. This data can also help to develop tracer displacement statistics and models for this type of river with respect to morphologic change and bar development.

The intrabedform, or intrabar, transport that was observed on the San Juan River, aligns with results from the few previous bedload tracking results on larger, bar-dominated channels. On a meandering section of the Ain River, France, Rollet et al. (2008) conducted a PIT tag tracer study, recovering 36 % of tracers after one year, with an average travel distance of 50 m, less than one bar length downstream. While interpretation of particle transport was limited by the low recovery rate, the authors noted that over the tracer monitoring period, a thick sedimentary layer had accreted on the edge of the gravel bar immediately downstream of the tracer injection site and posited that lost tracers were likely buried at this location, beyond their antenna's maximum range of detection. This description of bar growth is similar to changes observed on Bar 6 of the San Juan River, where tracer clustering and lateral accretion was focused at the bar apex. In another PIT tag study, conducted on a wandering riffle-pool reach of the Durance River, France, Chapuis et al. (2015) recovered 40 % of tracers after four months, with an average particle path length of 83 m, again indicative of transport within one riffle-pool unit. As observed on the San Juan River, the authors noted that particles deployed on bar tails were either immobile or only displaced short distances, while those seeded closer to the thalweg were transport farther downstream. Similar variations in transport conditions between morphologic units were reported from PIT tag and painted tracer data collect from a wandering reach of the Parma River, Italy (Brenna et al., 2019). The spatial variability in bedload transport, intrinsic to the riffle-pool morphology, means that deployment strategy has a strong influence on tracer mobility and resultant path length distributions. In the cases of the Ain, Durance, and San Juan Rivers, tracers tended to remain within one morphological unit, with minimal transport downstream. This provides direct evidence that in addition to hydraulic controls, channel morphology influences particle dynamics in these systems. Particle trapping and burial in association with bar development appears to be an important consideration in modeling sediment behaviour in this type of river, and therefore in the bedload transport process more generally. This emphasizes the

morphologic control on bed particle transport, a point that was also raised in a re-analysis of bedload tracking data by both Vázquez-Tarrío et al. (2018) and McDowell and Hassan (2020).

The pattern of particle displacement and deposition on the San Juan River reflected a combination of morphologic controls and seasonal variations in the flow regime. During the 2017-18 winter, the wettest study year, bedload deposition focused at the apex of the first bar downstream for Bars 7 and 15, and either slightly positive or symmetrical distributions around the bar apex were observed. However, during years with more moderate floods and lower competent flow volume, path length distributions tended to be positively skewed, with lower tracer mobility. It should be noted here that these results specifically pertain to particles seeded on the bed surface near the bar head. At least this is the case for the first movement of tracers, while subsequent events in the same year could be acting on both surficial and buried tracers. Differences in the spatial distribution of tracers between sites also appears related to channel shape and bar morphology. At Bar 6, the high-amplitude bend, and migration of a coarse bedload sheet, appear to restrict transport to the bar tail. Whereas tracer deposition on the bar tail was more common for Bars 7 and 15, bars that are less well-developed laterally. Overall, the results from this study provide some validation to the findings from Pyrce and Ashmore's flume experiments (2003a; 2005) whereby they observed bi- and multi-modal path length distributions during bar-forming discharges, with modes coincident with bar apexes, and spatial patterns of tracer deposition related to bar-scale patterns of erosion and deposition.

To further compare tracer transport on the San Juan River with results from the literature, Figure 4 from Vázquez-Tarrío et al. (2018), has been re-created in Figure 21 with data from Bars 6, 7, and 15 on the San Juan River. The original figure contains travel distances of tracers starting from both unconstrained (i.e. initial movement after seeding, as done in this study) and constrained (movement after tracers have been incorporated into the bed) positions. In this graph, dimensionless stream power (ω^*) was calculated as in Eaton and Church (2011), to compare flow strength and particle transport across rivers of different scales. Mean scaled travel distances were scaled using a morphologic length scale (i.e. the spacing of macroscale bedforms), which for the San Juan River meant the riffle-riffle spacing. Data from the 2015-16 deployment on Bar 6 were not plotted on this graph due to the low recovery rate (33 %) and uncertainty in the statistics of particle displacement for this year. The San Juan River data appear in line with results from riffle-pool channels, showing a positive relationship between dimensionless stream power and mean scaled travel distance, though travel distances on the San Juan River were relatively low (Figure 21). What is more interesting though, and as noted by Vázquez-Tarrío et al. (2018), is that riffle-pool channels share a common trait in that they rarely exhibit average travel distances beyond 1-2 length-scale units (regardless of constrained or unconstrained starting position), generally at the lower end of the range for other channel types. It appears that riffle-pool channels have limited transport distances compared with other channels, presumably a result of bars and riffles constraining particle movement. Over the long-term, path lengths are therefore likely to be limited by the rate of bar development and re-working, which in turn plays an important role in overall channel evolution and stability (Rice et al., 2009; Reid et al., 2019).

The path length distributions presented in this study reflect annual particle transport over a four year period. The annual displacements occur from multiple events in the well-defined high-flow season from October to March. This is consistent each year although exact magnitudes vary. Particles are 'slaved' to the bar development and few move through to the next bar any given year. The preferential deposition and incorporation of tracers in bars has been previously

demonstrated to hold true over longer time-scales in gravel-bed rivers in general (e.g. Ferguson et al., 2002; Haschenburger, 2013). Therefore, we expect that these annual path lengths are representative of the normal bar development except in the case of a high magnitude flood sufficient to disrupt the existing bar and channel configuration, in which case displacements would be expected to reflect that larger scale morphological change. For morphological flux calculation this would produce an annual flux based on net morphological change and tracer distances scaled to the bars.

The tracer burial data provide context to the path length analysis and revealed insights into patterns of sediment transfer and storage. Burial depths up to, and likely exceeding, 50 cm were recorded at each of the three sites, although the absolute magnitude of maximum particle burial depth was not obtained in this study due to methodological constraints. However, the development of "wobblestone" technology looks to provide a promising solution to estimating particle burial without the need to physically recover the particles and disturb the bed (Papangelakis et al., 2019). Overall, tracer burial aligned with the patterns of bar-scale deposition observed on DoDs, which raises two important points. First, this suggests that as individual particles are transported to and buried in local areas of deposition, they become incorporated into the channel morphology, and future movement will be limited by the rate of bedform (or bar) migration. This relates back to Neill's (1987) original speculation that over the long term, average particle path lengths may be inferred from the channel morphology. Secondly, the fact that more than 30 % of buried tracers were recovered at depths beyond twice the local D_{90} for each site suggests that the concept of a shallow active layer less than two particles deep does not reflect the nature of bedload processes occurring in this type of channel. It should be noted however, that the winter storm season was treated as a single event for this study, and that there were multiple events each year that may have produced the reported burial depths. As described by Ashmore et al. (2018), it appears that bed particle deposition and burial in larger, more dynamic rivers is controlled by bar-scale patterns of deposition, whereby the active layer is spatially non-uniform and maximum burial depths occur on the scale of vertical changes in bed level associated with those dominant morphological processes. This is important because the dimensions of the active layer, when combined with the virtual velocity of bed particles, gives the morphological bedload transport rate (Haschenburger and Church, 1998; Liébault and Laronne, 2008; Vázquez-Tarrío and Menéndez-Duarte, 2014; Mao et al. 2017; Vericat et al., 2017).

5 Conclusion

Annual tracking of bed particles over four years in a large bar-dominated wandering gravel-bed river, combined with repeat LiDAR surveys of topographic change, show that particle displacements are closely tied to the bar scale of the river and to patterns of bar development and accretion. This has implications for annual and event-based path length when applied to virtual velocity and morphological estimates of bedload, and points to possible differences in path length characteristics and controls between rivers of different morphology and size.

Annual tracer path lengths were tied directly to the local channel morphology with tracer deposition and burial reflected by areas of deposition on DEMs of difference (DoDs) over the time period of tracer tracking. Year to year differences in tracer path lengths related to the annual flow regime were also observed, though appear secondary to morphologic constraints because tracers were rarely transported past the bar immediately downstream of their injection site.

Tracer deposition focused along bar margins and to a lesser extent, the surface of the downstream portion of bars, reflecting the downstream bar migration and lateral bar accretion observed on DoDs. Burial information indicates that active layer depths are tied to topographic change and exceed the grain exchange depth that is typically assumed in bedload analysis and modeling in gravel-bed rivers. This highlights the fundamental importance of bar development and re-working underpinning bedload transport processes in bar-dominated channels and supports recent analyses of morphological effects in tracer dispersion as indicated by Vázquez-Tarrío et al. (2018). Ultimately, short-term particle displacements in bar-dominated channels are linked with the morphological style of channel evolution and therefore differs from bedload processes in small, plane-bed channels, for which much previous analysis and theory have been developed.

Acknowledgments, Samples, and Data

This work was funded by the British Columbia Ministry of Forests, Lands, Natural Resource Operations and Rural Development (FLNRORD) and the Pacheedaht First Nation. The data used in this study can be found in the Scholars Portal Dataverse (https://doi.org/10.5683/SP2/UQGZCG). We are thankful to Jesse Schafer for preparation of GIS data, and the following persons for their field support: Andrew Boxwell, Spencer Ranson, David Waine, Kyle Fukui, Dave Johnson, Ali Jones, Rachel Dugas, and several FLNRORD employees. We also thank BioMark for their feedback on optimising the RFID antenna setup. Finally, we would like to thank three anonymous reviewers for their thoughtful and constructive comments on the original manuscript, as it has vastly improved the quality of the paper.

References

Arnaud, F., Piégay, H., Vaudor, L., Bultingaire, L., and Fantino, G. (2015). Technical specifications of low-frequency radio identification bedload tracking from field experiments: Differences in antennas, tags and operators. *Geomorphology, 238*, pp. 37-46.

Arnaud, F., Piégay, H., Béal, D., Collery, P., Vaudor, L., and Rollet, A. (2017). Monitoring gravel augmentation in a large regulated river and implications for process-based restoration. *Earth Surface Processes, 42*, pp. 2147-2166.

Ashmore, P.E., and Church, M. (1998). Sediment transport and river morphology: A paradigm for study. In P.C. Klingeman, R.L. Beschta, P.D. Komar, and J.B. Bradley (Eds.) *Gravel-Bed Rivers in the Environment* (pp. 115-148). Water Resources Publications, LLC, Highland Ranch, Colorado.

Ashmore, P., Peirce, S., and Leduc, P. (2018). Expanding the “active layer”: Discussion of Church and Haschenburger (2017) What is the “active layer?” *Water Resources Research* 53, 5-10, Doi:10.1002/2016WR019675. *Water Resources Research, 54*, pp. 1-3.

BC Geological Survey (2018). Bedrock geology [Shapefile]. Retrieved from: https://catalogue.data.gov.bc.ca/dataset/bedrock-geology/resource/aa3a15f8-02fe-49c6-836c-6866c326203d?inner_span=True

Beechie, T.J. (2001). Empirical predictors of annual bed load travel distance, and implications for salmonid habitat restoration and protection. *Earth Surface Processes and Landforms, 26*, pp. 1025-1034.

761 Beechie, T.J., Liermann, M., Pollock, M.M., Baker, S., and Davies, J. (2006). Channel pattern
762 and river-floodplain dynamics in forested mountain river systems. *Geomorphology, 78*, pp. 124-
763 141.

764 Bradley, D.N., and Tucker, G.E. (2012). Measuring gravel transport and dispersion in a
765 mountain river using passive radio tracers. *Earth Surface Processes and Landforms, 37*, pp.
766 1034-1045.

767 Brasington, J., Langham, J., Rumsby, B. (2003). Methodological sensitivity of morphometric
768 estimates of coarse fluvial sediment transport. *Geomorphology, 53,* pp. 299-316.

769 Brenna, A., Surian, N., and Mao, L. (2019). Virtual velocity approach for estimating bed
770 material transport in gravel-bed rivers: Key factors and significance. *Water Resources Research,*
771 *55*, pp. 1651-1674.

772 Brousse, G., Liébault, F., Arnaud-Fassetta, G., Vázquez-Tarrío, D. (2018). Experimental bed
773 active-layer survey with active RFID scour chains: Example of two braided rivers (the Drac and
774 the Vénéon) in the French Alps. *E3S Web of Conferences, 40*, 04016.

775 Cain, A., and MacVicar, B. (2020). Field tests of an improved sediment tracer inlucding non-
776 intrusive measurement of burial depth. *Earth Surface Processes and Landforms.*
777 *DOI*:10.1002/esp.4980.

778 Cassel, M., Piégay, H., and Lavé, J. (2017a). Effects of transport and insertion of radio frequency
779 identification (RFID) transponders on resistance and shape of natural and synthetic pebbles:
780 applications for riverine and coastal bedload tracking. *Earth Surface Processes and Landforms,*
781 *42*, pp. 399-413.

782 Cassel, M., Dépret, T., and Piégay H. (2017b). Assessment of a new solution for tracking
783 pebbles in rivers based on active RFID. *Earth Surface Processes and Landforms,*
784 DOI:10.1002/esp.4152.

785 Cassel, M., Piégay, H., Fantino, G., Lejot, J., Bultingaire, L., Michel, K., and Perret, F. (2020).
786 Comparison of ground-based and UAV a-UAF artificial tracer mobility monitoring methods on a
787 braided river. *Earth Surface Processes and Landforms, 45*, pp. 1123-1140.

788 Chapuis, M., Bright, C.J., Hufnagel, J., and MacVicar, B. (2014). Detection ranges and
789 uncertainty of passive Radio Frequency Identification (RFID) transponders for sediment tracking
790 in gravel rivers and coastal environments. *Earth Surface Processes and Landforms, 39*(15), pp.
791 2109-2120.

792 Chapuis, M., Dufour, S., Provansal, M., Couvert, B., and de Linares, M. (2015). Coupling
793 channel evolution monitoring and RFID tracking in a large, wandering, gravel-bed river: Insights
794 into sediment routing on geomorphic continuity through a riffle-pool sequence. *Geomorphology,*
795 *231,* pp. 258-269.

796 Church, M. (2006). Bed material transport and the morphology of alluvial river channels. *The*
797 *Annual Review of Earth and Planetary Science, 34*, pp. 325-354.

798 Church, M., and Ferguson, R.I. (2015). Morphodynamics: Rivers beyond steady state. *Water*
799 *Resources Research, 51*, pp. 1883-1897.

800 Church, M., and Hassan, M.A. (1992). Size and distance of travel of unconstrained clasts on a
801 streambed. *Water Resources Research, 28*, pp. 299-303.

802 Church, M., and Rice, S.P. (2009). Form and growth of bars in a wandering gravel-bed river.
803 *Earth Surface Processes and Landforms, 34*, pp. 1422-1432.

804 Desloges, J.R., and Church, M. (1987). Channel and floodplain facies in a wandering gravel-bed
805 river. In *Recent development in fluvial sedimentology, 39* (pp. 99-109). Society of Economic
806 Paleontologists and Mineralogists.

807 Eaton, B., Hassan, M., and Phillips, J. (2008). A Method for Using Magnetic Tracer Stones to
808 Monitor Changes in Stream Channel Dynamics. *Streamline: Watershed Management Bulletin,*
809 *12*(1), pp. 22-28.

810 Eaton, B., and Church, M. (2011). A rational sediment transport scaling relation based on
811 dimensionless stream power. *Earth Surface Processes and Landforms, 37*, pp. 901-910.

812 Environment and Climate Change Canada (2019). Canadian Climate Normals 1981-2010 Station
813 Data. Retrieved from:
814 http://climate.weather.gc.ca/climate_normals/results_1981_2010_e.html?stnID=82&autofwd=1

815 Ferguson, R.I., Bloomer, D.J., Hoey, T.B., and Werritty, A. (2002). Mobility of river tracer
816 pebbles over different timescales. *Water Resources Research, 38*(5), pp. 3-1 – 3-8.

817 Fuller, I.C., Large, A.R.G., and Milan, D.J. (2003). Quantifying channel development and
818 sediment transfer following chute cutoff in a wandering gravel-bed river. *Geomorphology, 54,*
819 pp. 307-323.

820 Haschenburger, J.K. (2013). Tracing river gravels: Insights into dispersion from a long-term field
821 experiment. *Geomorphology, 200*, pp. 121-131.

822 Haschenburger, J.K., and Church, M. (1998). Bed material transport estimated from the virtual
823 velocity of sediment. *Earth Surface Processes and Landforms, 23*, pp. 791-808.

824 Hassan, M.A., and Bradley, D.N. (2017). Geomorphic controls on tracer particle dispersion in
825 gravel bed rivers. In D. Tsutsumi, and J.B. Laronne (Eds.) *Gravel Bed Rivers: Processes and*
826 *Disasters, 1* (pp. 159-184). John Wiley & Sons Ltd.

827 Hassan, M.A., and Roy, A.G. (2016). Coarse particle tracking in fluvial geomorphology. In G.M.
828 Kondolf, and H. Piégay (Eds.) *Tools in Fluvial Geomorphology. Second Edition* (pp. 306-323).
829 Chichester, West Sussex England: Wiley Blackwell.

830 Hassan, M.A., Church, M., and Ashworth, P.J. (1992). Virtual rate and mean distance of travel of
831 individual clasts in gravel-bed channels. *Earth Surface Processes, 17*, pp. 617 - 627.

832 Kasprak, A., Wheaton, J.M., Ashmore, P.E., Hensleigh, J.W., and Peirce, S. (2015). The
833 relationship between particle travel distance and channel morphology: Results from physical
834 models of braided rivers. *Journal of Geophysical Research: Earth Surface, 120*, pp. 55-74.

835 Lamarre, H., MacVicar, B., and Roy, A.G. (2005). Using passive integrated transponders (PIT)
836 tags to investigate sediment transport in gravel-bed rivers. *Journal of Sedimentary Research, 75,*
837 pp. 736-741.

838 Liébault, F., and Laronne, J.B. (2008). Evaluation of bedload yield in gravel-bed rivers using
839 scour chains and painted tracers: the case of the Esconavette Torrent (Southern French Prealps).
840 *Geodinamica Acta, 21*, pp. 23-34.

Liébault, F., Bellot, H., Chapuis, M., Klotz, S., and Deschâtres, M. (2012). Bedload tracing in a high-sediment-load mountain stream. *Earth Surface Processes and Landforms, 37*, pp. 385-399.

Mao, L., Picco, L., Lenzi, M.A., and Surian, N. (2017). Bed material transport estimate in large gravel-bed rivers using the virtual velocity approach. *Earth Surface Processes and Landforms, 42*, pp. 595-611.

McDowell, C., and Hassan, M.A. (2020). The influence of channel morphology on bedload path lengths: Insights from a survival process model. *Earth Surface Processes and Landforms*. DOI: 10.1002/esp/4946.

McLean, D.G., Church, M., and Tassone, B. (1999). Sediment transport along lower Fraser River 1. Measurements and hydraulic computations. *Water Resources Research, 35*(8), pp. 2533-2548.

Middleton, L., Ashmore, P., Leduc, P., and Sjogren, D. (2019). Rates of planimetric change in a proglacial gravel-bed braided river: Field measurement and physical modelling. *Earth Surface Processes and Landforms, 44*, pp. 752-765.

Milan, D.J. (2013). Virtual velocity of tracers in a gravel-bed river using size-based competence duration. *Geomorphology, 198*, pp. 107-114.

Misset, C., Recking, A., Legout, C., Bakker, M., Bodereau, N., Borgniet, L., Cassel, M., Geay, T., Gimbert, F., Navratil, O., Piegay, H., Valsangkar, N., Cazilhac, M., Poirel, A., and Zanker, S. (2020). Combining multi-physical measurements to quantify bedload transport and morphodynamics interactions in an alpine braiding river reach. *Geomorphology, 351*.

Mollard, J.D. (1973). Airphoto interpretation of fluvial features. In *Fluvial processes and sedimentation. National Research Council of Canada, Ottawa, ON* (pp. 341-380). Inland Waters Directorate, Department of the Environment.

Montgomery, D.R., and Buffington, J.M. (1997). Channel-reach morphology in mountain drainage basins. *Geological Society of America Bulletin*, pp. 596 – 611.

Neill, C.R. (1973). Hydraulic and morphologic characteristics of Athabasca River near Fort Assiniboine (pp. 1-23). Alberta Research Council, Edmonton, Highway and River Engineering Division Report REH/73/7.

Neill, C.R. (1987). Sediment balance considerations linking long-term transport and channel processes. In C.R. Thorne, J.C. Bathurst, and R.D. Hey (Eds.) *Sediment Transport in Gravel-Bed Rivers* (pp. 225-239). John Wiley & Sons Ltd.

Northwest Hydraulic Consultants Ltd. (1994). Impact of forest harvesting in terrain stability, stream channel morphology and fisheries resources of the San Juan River Watershed, Vancouver Island. http://a100.gov.bc.ca/pub/acat/public/viewReport.do?reportId=23277

O'Connor, J.E., Jones, M.A., and Haluska, T.L. (2003). Flood plain and channel dynamics of the Quinault and Queets Rivers, Washington, USA. *Geomorphology, 51*, pp. 31-59.

Papangelakis, E., and Hassan, M., (2016). The role of channel morphology on the mobility and dispersion of bed sediment in a small gravel-bed stream. *Earth Surface Processes and Landforms, 41*, pp. 2191-2206.

Papangelakis, E., Muirhead, C., Schneider, A., and MacVicar, B. (2019). Synthetic Radio Frequency Identification tracer stones with weighted inner ball for burial depth estimation.

Journal of Hydraulic Engineering, 145(12), 06019014. https://doi.org/10.1061/(ASCE)HY.1943-7900.0001650

Pfeiffer, A.M., Finnegan, N.J., and Willebring, J.K. (2017). Sediment supply controls equilibrium channel geometry in gravel rivers. *Proceedings of the National Academy of Sciences, 114*(13), pp. 3346-3351.

Phillips, C.B., and Jerolmack, D.J. (2014). Dynamics and mechanics of bed-load tracer particles. *Earth Surface Dynamics, 2*, pp. 513-530.

Phillips, C.B., and Jerolmack, D.J. (2019). Bankfull transport capacity and the threshold of motion in coarse-grained rivers. *Water Resources Research, 55*, pp. 11316-11330.

Peirce, S.E.K. (2017). Morphological bedload transport in gravel-bed braided rivers. *Electronic Thesis and Dissertation Repository*. 4595. https://ir.lib.uwo.ca/etd/4595

Pyrce, R.S., and Ashmore, P.E. (2003a). Particle path length distributions in meandering gravel-bed streams: Results from physical models. *Earth Surface Processes and Landforms, 28*, pp. 951-966.

Pyrce, R.S., and Ashmore, P.E. (2003b). The relation between particle path length distributions and channel morphology in gravel-bed streams: a synthesis. *Geomorphology, 56*, pp. 167-187.

Pyrce, R.S., and Ashmore, P.E. (2005). Bedload path length and point bar development in gravel-bed river models. *Sedimentology, 52*, pp. 839-857.

Reid, H.E., Williams, R.D., Brierley, G.J., Coleman, S.E., Lamb, R., Rennie, C.D., and Tancock, M.J. (2019). Geomorphological effectiveness of floods to rework gravel bars: Insight from hyperscale topography and hydraulic monitoring. *Earth Surface Processes and Landforms, 44*, pp. 595-613.

Rice, S.P., Church, M., Woolridge, C.L., and Hickin, E.J. (2009). Morphology and evolution of bars in a wandering gravel-bed river; Lower Fraser River, British Columbia, Canada. *Sedimentology, 56*, pp. 709-736.

Rollet, A.J., MacVicar, B., Piégay, H., Roy, A.G. (2008). A comparative study on the use of passive integrated transponders to estimate sediment transport: first results (in French). *La Houille Blanche, 4*, pp. 110-116.

Ryan, S.E., Porth, L.S., and Troendle, C.A. (2002). Defining phases of bedload transport using piecewise regression. *Earth Surface Processes and Landforms, 27*, pp. 971-990.

Schneider J., Hegglin, R., Meier, S., Turowski, J.M., Nitsche, M., and Rickenmann, D. (2010) Studying sediment transport in mountain rivers by mobile and stationary RFID antennas. In A. Dittrich, K. Koll, J. Aberle, and P. Geisenhainer (Eds.) *River Flow* (pp. 1723-1730). Karlsruhe: Bundesanstalt für Wasserbau. S.

Terra Remote Sensing Inc. (2018a). Project report: Renfrew. September 4, 2018. (pp. 1-29). Sidney, BC.

Terra Remote Sensing Inc. (2018b). Project report: Aerial LiDAR and imagery survey at San Juan River, Vancouver Island, BC. April 24, 2018. (pp. 1-51). Sidney, BC.

Terra Remote Sensing Inc. (2019). Project report: Juan River change detection survey. Port Renfrew, BC. November 12, 2019. (pp. 1-45). Sidney, BC.

Tomsett, C., and Leyland, J. (2019). Remote sensing of river corridors: A review of current trends and future directions. *River Research and Applications*, pp. 1-25.

Vázquez-Tarrío, D., and Batalla, R.J. (2019). Assessing controls on the displacement of tracers in gravel-bed rivers. *Water, 11*, pp. 1-21.

Vázquez-Tarrío, D., and Menéndez-Duarte, R. (2014). Bedload transport rates for coarse-bed streams in an Atlantic region (Narcea River, NW Iberian Peninsula). *Geomorphology, 217*, pp. 1-14.

Vázquez-Tarrío, D., Recking, A., Liébault, F., Tal, M., and Menéndez-Duarte, R. (2018). Particle transport in gravel-bed rivers: Revisiting passive tracer data. Earth Surface Processes and Landforms, 44, pp. 112-128.

Vericat, D., Wheaton, J.M., and Brasington, J. (2017). Revisiting the morphological approach. In D. Tsutsumi and J.B. Laronne (Eds.) *Gravel Bed Rivers: Processes and Disasters, 1* (pp. 121-158). John Wiley & Sons Ltd.

Water Survey of Canada (2019). Monthly Discharge Data for SAN JUAN RIVER NEAR PORT RENFREW (O8HA010) [BC]. Retrieved from: https://wateroffice.ec.gc.ca/report/historical_e.html?stn=08HA010&mode=Table&type=h2oArc&results_type=historical&dataType=Monthly&parameterType=Flow&year=2017&y1Max=1&y1Min=1

Wheaton, J.M., Brasington, J., Darby, S.E., and Sear, D.A. (2010). Accounting for uncertainty in DEMs from repeat topographic surveys: improved sediment budgets. *Earth Surface Processes and Landforms, 35*, pp. 135-156.

Wilcock, P.R., and McArdell, B.W., (1997). Partial transport of a sand/gravel sediment. *Water Resources Research, 33*, pp. 235-245.

Wolman, M.G. (1954). A method of sampling coarse river-bed material. *Transactions, American Geophysical Union, 35*(6), pp. 951-956.

Figure 1. Location of **(a)** the San Juan River watershed and **(b)** study sites for tracer monitoring.

Figure 2. San Juan River annual flood frequency (data sourced from WSC, 2019).

Figure 3. Grain size distributions for surface bed-material and tracers for **(a)** Bar 6, **(b)** Bar 7, and **(c)** Bar 15.

Figure 4. Antennas used during tracer recovery surveys. Panel **(a)** shows the BP Plus Portable wand antenna, and panel **(b)** shows the Cord Antenna System.

Figure 5. Time-lapse imagery of the apex of Bar 6 on **(a)** September 18th, 2017 at 1:45 pm. The hydrometric station recorded a discharge of 1.2 m^3/s at the time of this image. The apex of Bar 6 on **(b)** November 19th, 2017 at 3:45 pm. The hydrometric station recorded a discharge of 560.4 m^3/s at the time of this image.

Figure 6. San Juan River hydrograph from September 2015 to September 2019. Data from WSC, 2019.

Figure 7. **(a)** Relative tracer mobility, **(b)** median scaled path length, and **(c)** mean burial depth, plotted against total excess flow energy. Path length data are scaled by the length of the bar at which they were seeded.

Figure 8. Path length frequency distribution for **(a)** Bar 6, **(b)** Bar 7, and **(c)** Bar 15 mobile tracers (i.e. transported more than 10 m downstream).

Figure 9. Tracer recovery locations for Bar 6 deployed in **(a)** 2015, **(b)** 2016, **(c)** 2017, and **(d)** 2018. Note that these maps include tracers recovered in surveys two or more years after deployment.

Figure 10. Tracer recovery locations for Bar 7 deployed in **(a)** 2016, **(b)** 2017, and **(c)** 2018. Note that these maps include tracers recovered in surveys two or more years after deployment.

Figure 11. Tracer recovery locations for Bar 15 deployed in **(a)** 2016, **(b)** 2017, and **(c)** 2018. Note that these maps include tracers recovered in surveys two or more years after deployment.

Figure 12. Box plots of scaled tracer path lengths for each study site. Note: n_m is the number of mobile tracers; the box represents the 25th and 75th percentiles; the line inside the box is the median; vertical lines represent the 10th and 90th percentiles; black dots represent the maximum observed path length. Path length data are scaled by the length of the bar at which they were seeded.

Figure 13. Planform view of the migrating bedload sheet at the apex of Bar 6 (from 2017). Inset shows the one-metre tall slip face at the downstream extent of the sheet

Figure 14. Box plots of scaled tracer path lengths as a function of initial morphologic unit. Note: the box represents the 25th and 75th percentiles; the line inside the box is the median; vertical lines represent the 10th and 90th percentiles. Path length data are scaled by the length of the bar at which they were seeded.

Figure 15. Tracer burial for Bar 6 and Bar 7. The position of buried tracers that were recovered between 2015 and 2018 are overlaid on the corresponding DoD in the upper panel. Those recovered in 2019 are shown in the lower panel overtop of the 2018-2019 DoD.

Figure 16. Tracer burial for Bar 15. The position of buried tracers that were recovered between 2015 and 2018 are overlaid on the corresponding DoD in the upper panel. Those recovered in 2019 are shown in the lower panel overtop of the 2018-2019 DoD.

Figure 17. Tracer burial depths for **(a)** Bar 6, **(b)** Bar 7, and **(c)** Bar 15.

Figure 18. Tracer burial depth plotted against net elevation change in the DoD for the cell in which the tracer was buried.

Figure 19. Tracer path lengths (L) as a function of scaled grain size (D) for each size fraction of tracers. Path length is scaled by the mean path length of the size fraction containing the local D_{50}. Grain size is scaled by the D_{50} of local bed surface material. Coloured dots represent data summarized for a specific size fraction of tracers, hollow grey dots represent the raw data. Note that previous studies have scaled particle size by the local subsurface D_{50}, whereas the San Juan data was scaled by the local surface D_{50} as no bulk grain size sampling was carried out.

Figure 20. Relative tracer mobility plotted as a function of grain size for each tracer size fraction across all study sites. Grain size is scaled by the D_{50} of local surface bed material.

Figure 21. Mean scaled travel distance as a function of dimensionless stream power for various channel types and the San Juan River. This figure is re-created from Figure 4 in Vázquez-Tarrío et al. (2018). San Juan River path lengths are scaled by the distance between successive riffles.

Table 1. Dimensions of study bars. Bar length was measured relative to the channel thalweg. All measurements are based on 2015 Lidar DEMs.

Location	Length (m)	Average Width (m)	Relief (m)	Slope (m m^{-1})
Bar 6	550	100	4.2	0.0038
Bar 7	540	55	3.9	0.0031
Bar 15	585	45	3.2	0.0009

Table 2. Grain size data for tracers and surficial bed material.

Location	b-axis percentile	Grain Size (mm)		
		Tracers	Bed Material	Bed Material (Truncated)
Bar 6	D_{16}	28-39	26	32
	D_{50}	45-54	50	55
	D_{84}	73-87	84	86
Bar 7	D_{16}	28-29	16	34
	D_{50}	45-46	43	56
	D_{84}	73-74	87	97
Bar 15	D_{16}	28-30	8	27
	D_{50}	45-51	28	42
	D_{84}	73-82	67	87

Table 3. Lidar survey metadata (sourced from TRS Inc., 2018a,b, 2019). Note: $RMSE_v$ – vertical root mean square error, σ_v – standard deviation of vertical error.

Year of Survey	$RMSE_v$ (m)	σ_v (m)	Average point density (points/m^2)
2015	0.026	0.036	12.8 ± 7.2
2018	0.032	0.037	28 ± 16.0
2019	0.069	0.062	38 ± 11.0

Table 4. Summary of annual floods and tracer recovery results. Mobility rate is calculated as the fraction of tracers that were recovered more than ten metres downstream of their initial position. Tracer path lengths are scaled by the length of the bar at which they were seeded. Average burial depths include surface tracers.

	Number of Events $Q>Q_{bf}$	Maximum Peak Discharge, Q_{max} ($m^3 s^{-1}$)	Total Excess Flow Energy, Ω_T ($MJ m^{-1}$)	Recovery Rate, R (%)	Mobility Rate, r_m	Median Path Length (m)	Median Scaled Path Length, L_{50}	Maximum Scaled Path Length, L_{max}	Average Burial Depth, B_{avg} (cm)
Bar 6									
2015-16	6	1,022	571	33	0.82	38	0.07	0.46	9.8
2016-17	4	749	331	66	0.89	69	0.12	0.78	5.7
2017-18	6	1,003	890	71	0.91	130	0.23	2.02	16.4
2018-19	5	942	479	75	0.88	155	0.28	0.79	19.6
Bar 7									
2016-17	4	749	331	76	0.80	97	0.18	0.92	4.4
2017-18	6	1,003	890	69	0.87	187	0.35	0.94	14.9
2018-19	5	942	479	79	0.93	219	0.41	1.41	13.0
Bar 15									
2016-17	4	749	180	70	0.48	155	0.27	0.96	5.1
2017-18	6	1,003	483	65	0.92	308	0.54	1.27	8.4
2018-19	5	942	260	75	0.94	197	0.32	1.34	8.5

Table 5. Tracer mobility and path length data aggregated across all years of tracer deployment for each study site.

	Bar 6	Bar 7	Bar 15
n_m	259	250	218
r_m	0.89	0.87	0.78
L_{50}	0.22	0.34	0.40
$n_{L>1.0}$	1	12	8
$r_{L>1.0}$	0.00	0.05	0.04
L_{max}	2.02	1.41	1.34

Note: n_m – number of mobile tracers, r_m – mobility rate, L_{50} – median scaled path length, $n_{L>1.0}$ – number of tracers transported more than one bar length downstream, $r_{L>1.0}$ – tracer escape rate, L_{max} – maximum observed scaled path length

1147 **Table 6.** Tracer mobility and path length breakdown by initial morphologic unit.

1148

Bar 6	Initial Morphologic Unit			Bar 6 (2016)	Initial Morphologic Unit	
	bar head	wetted channel	bar tail		bar edge	wetted channel
r_m	1.00	0.96	0.77	r_m	0.75	0.96
L_{50}	0.27	0.21	0.21	L_{50}	0.11	0.17
L_{max}	0.86	0.92	2.02	L_{max}	0.28	0.78

Bar 7	Initial Morphologic Unit		Bar 15	Initial Morphologic Unit		
	wetted channel	bar tail		bar head	wetted channel	bar tail
r_m	0.94	0.82	r_m	0.98	0.73	0.80
L_{50}	0.39	0.21	L_{50}	0.50	0.42	0.27
L_{max}	1.24	1.41	L_{max}	0.93	1.27	1.34

1149
1150
1151
1152
1153
1154
1155
1156
1157
1158
1159
1160
1161
1162
1163
1164
1165
1166
1167
1168
1169
1170
1171
1172
1173
1174
1175
1176
1177

Table 7. Summary of net elevation changes on bar surfaces for 2015-18 and 2018-19 DoDs. The percentage of erosion and deposition reflects the relative proportion of cells that were net depositional and erosional on bar surfaces. Average erosion and deposition values are likely to be inflated relative to the true changes occurring on bar surfaces, as the change detection algorithm better captures high-magnitude changes compared to low-magnitude changes which may be indistinguishable from noise.

Location	2015-18		2018-19	
	% Erosion	% Deposition	% Erosion	% Deposition
Bar 6	20	80	7	93
Bar 7	11	89	4	96
Bar 15	23	77	14	86

Location	Net Elevation Change (m)							
	2015-18				2018-19			
	$Eros_{Avg}$	$Eros_{Max}$	Dep_{Avg}	Dep_{Max}	$Eros_{Avg}$	$Eros_{Max}$	Dep_{Avg}	Dep_{Max}
Bar 6	-0.47	-2.02	0.59	2.14	-0.70	-3.45	0.41	1.71
Bar 7	-0.45	-1.41	0.42	1.12	-0.48	-2.24	0.41	1.16
Bar 15	-0.45	-2.79	0.34	1.61	-0.72	-3.85	0.43	1.64

1211 **Table 8.** Summary of tracer recovery in areas of topographic change. Note: the fraction of
1212 recovered tracers in brackets reflect recovery in areas of known topographic change (i.e. tracers
1213 deposited in areas of indeterminate change removed).
1214

Location	Net Change in DoD				
	Indeterminate	Erosion		Deposition	
	Fraction of Recovered Tracers	Fraction of Recovered Tracers	B_{avg} (cm)	Fraction of Recovered Tracers	B_{avg} (cm)
Bar 6	0.51	0.06 (0.12)	12.1	0.43 (0.88)	18.5
Bar 7	0.35	0.06 (0.09)	5.1	0.59 (0.91)	10.3
Bar 15	0.73	0.08 (0.30)	5.7	0.19 (0.70)	10.6

1215
1216